nature structural & molecular biology

Article

https://doi.org/10.1038/s41594-022-00918-0

Structure and dynamics of the essential endogenous mycobacterial polyketide synthase Pks13

Received: 8 February 2022

Accepted: 21 December 2022

Published online: 13 February 2023

Check for updates

Sun Kyung Kim[1,9], Miles Sasha Dickinson[1,2,9], Janet Finer-Moore[1], Ziqiang Guan[3], Robyn M. Kaake[4,5,6], Ignacia Echeverria[5,6], Jen Chen[1], Ernst H. Pulido[4], Andrej Sali[7], Nevan J. Krogan[4,5,6], Oren S. Rosenberg[1,8] ✉ & Robert M. Stroud[1,2] ✉

The mycolic acid layer of the *Mycobacterium tuberculosis* cell wall is essential for viability and virulence, and the enzymes responsible for its synthesis are targets for antimycobacterial drug development. Polyketide synthase 13 (Pks13) is a module encoding several enzymatic and transport functions that carries out the condensation of two different long-chain fatty acids to produce mycolic acids. We determined structures by cryogenic-electron microscopy of dimeric multi-enzyme Pks13 purified from mycobacteria under normal growth conditions, captured with native substrates. Structures define the ketosynthase (KS), linker and acyl transferase (AT) domains at 1.8 Å resolution and two alternative locations of the N-terminal acyl carrier protein. These structures suggest intermediate states on the pathway for substrate delivery to the KS domain. Other domains, visible at lower resolution, are flexible relative to the KS-AT core. The chemical structures of three bound endogenous long-chain fatty acid substrates were determined by electrospray ionization mass spectrometry.

Mycobacterium tuberculosis (*Mtb*) coevolved with humans and is currently the world's most lethal bacterium, causing over 1.3 million deaths in 2020 (ref. [1]). In *Mtb* and other mycobacteria including the nonpathogenic *Mycobacterium smegmatis* (*Ms*), the outer layer of the cell envelope is a waxy, roughly 80 Å thick mycomembrane[2–4] primarily composed of 2-alkyl, 3-hydroxy long-chain fatty acids termed mycolic acids. This outer layer is essential for mycobacterial viability as it is the principal permeability barrier against environmental stressors including innate immune molecules and antimycobacterial drugs. Because of their central role in mycobacterial physiology, the reactions in the mycolic acid synthesis pathway are targets for antimycobacterial drugs[5]. Drugs that target earlier parts of the pathway in *Mtb* include the front-line drug isoniazid and thioamides such as ethionamide. While most strains of *Mtb* are susceptible to the standard regimen antibiotics, approximately half a million people are diagnosed with multi-drug resistant tuberculosis each year[6]. Hence steps in the pathway

[1]Department of Biochemistry and Biophysics, University of California San Francisco, San Francisco, CA, USA. [2]Chemistry and Chemical Biology Graduate Program, University of California San Francisco, San Francisco, CA, USA. [3]Department of Biochemistry, Duke University Medical Center, Durham, NC, USA. [4]Gladstone Institute of Data Science and Biotechnology, J. David Gladstone Institutes, San Francisco, CA, USA. [5]Department of Cellular and Molecular Pharmacology, University of California San Francisco, San Francisco, CA, USA. [6]Quantitative Biosciences Institute, University of California San Francisco, San Francisco, CA, USA. [7]Department of Bioengineering and Therapeutic Sciences, University of California San Francisco, San Francisco, CA, USA. [8]Department of Medicine, Division of Infectious Diseases, University of California San Francisco, San Francisco, CA, USA. [9]These authors contributed equally: Sun Kyung Kim, Miles Sasha Dickinson. ✉e-mail: Oren.Rosenberg@ucsf.edu; stroud@msg.ucsf.edu

of mycolic acid synthesis are pursued for new effective small molecule antimycobacterial drugs that can evade currently evolved drug resistance in *Mtb*[7,8].

The final steps of mycolic acid synthesis ligate two very long-chain fatty acid chains together in a condensation step carried out by a multidomain polyketide synthase 13 (Pks13)[9] to form an α-alkyl β-ketoacyl thioester (Supplementary Fig. 1). Each Pks13 polypeptide chain begins with an acyl carrier protein (ACP) toward the N terminus (ACP1) (Fig. 1a,b) that is activated by attachment of a 4′-phosphopantetheinyl prosthetic group (Ppant, **1**), to S38 of the ACP1 domain. One of the substrates of Pks13 is generated from a long-chain fatty acid R1, containing aliphatic chains between 48 and 62 carbons in length. AMP ligase FadD32 activates R1 by AMPylating the substrate to produce meromycolyl-AMP, **2** (refs. [10–13]). This meromycolyl-AMP is the equivalent of a 'starter unit' in a modular PKS. The terminal thiol of the Ppant group on ACP1 displaces the AMP to form a thioester with the R1 meromycolyl chain, **3**. This process also requires FadD32 in a role analogous to the loading domain in other PKSs[10,12,14] (Fig. 1b). In the amino acid sequence of Pks13 the ACP1 domain is followed by a KS domain (Fig. 1a). The meromycolyl chain attached to ACP1 *trans*-thioesterifies on to C267 of the KS domain in preparation for the subsequent chain extension (Fig. 1b).

The second substrate is derived from a long-chain fatty acid R2 containing aliphatic chains between 24 and 26 carbons in length. R2 is first esterified by coenzyme A (CoA) and carboxylated by an acyl-CoA-carboxylase AccD4, to yield an α-carboxy-acyl-CoA, **4** (Fig. 1b). This product is analogous to the 'extender unit' of modular PKSs. It is notable that the genes that encode FadD32 and AccD4 flank the gene for Pks13 (Fig. 1a).

A 159 amino acid linker domain follows KS in the Pks13 chain and leads into the acyl transferase (AT) domain. Serine S798 of the AT domain displaces CoA to form a serine ester with the carboxyl of R2, **5**. The AT is followed by a 186-residue AT-ACP2 linker to a second Ppant-activated ACP (ACP2). R2 is captured by the sulfhydryl of the Ppant prosthetic group on ACP2 for transport to the KS active center where it undergoes a decarboxylative Claisen condensation with the R1 meromycolyl chain. The condensed product results in a mycolic α-alkyl β-ketoacyl thioester, **6** attached to the Ppant arm of ACP2. This intermediate is transferred from ACP2 to a thioesterase (TE) domain at the C terminus of Pks13, which ligates the condensed product to trehalose, **7**. Subsequently, the reductase CmrA reduces the ketone on the ligated intermediate to generate a mature trehalose monomycolic acid (TMM, **8**) (Fig. 1b and Supplementary Fig. 1a)[15]. A third ACP-like domain (ACP3) is also encoded in the Pks13 sequence although it does not contain the active site serine necessary for attachment of the Ppant prosthetic group. As ACP3 thus cannot perform the carrier function, its function in Pks13 remains unknown (Fig. 1a).

Although Pks13 is essential for *Mtb* there are no drugs yet that target individual enzymatic domains of Pks13. Furthermore, the general mechanism for how long-chain substrates are chaperoned and moved between domains has so far not been accessible for antimycobacterial target strategies[16]. We therefore sought to define the mechanism by which Pks13 processes these large hydrophobic substrates by determining the structure of the endogenous Pks13 purified from its in vivo state, with native long-chain substrates bound, rather than purified by overexpression in an exogenous host. This approach allowed us to visualize the multidomain enzyme in action and to uncover new functional sites in the substrate pathway that are unique to mycolic acid producing bacteria.

Results

Pks13 from native mycobacterial membranes is a stable dimer

Ms Pks13 shares 71% amino acid sequence identity with that of *Mtb*, carries out the same enzymatic reaction, and so is a model for Pks13 in the human pathogen *Mtb*[9]. The *pks13* locus was tagged at the C-terminal end of the endogenous gene in *Ms*[15] so as not to impair endogenous expression or function, with a tobacco etch virus (TEV)-cleavable green fluorescent protein GFP (Fig. 1a). The GFP fusion was used to enable native purification using anti-GFP nanobody beads.

Detergent was required for solubilization and purification, consistent with Pks13 being attached to the mycobacterial plasma membrane, as suggested based on live cell imaging[15]. Various detergents were evaluated for optimal solubilization of Pks13 using fluorescence size-exclusion chromatography (Methods), and *N*-dodecyl-β-D-maltoside (β-DDM, **9**) was selected based on efficiency of solubilization. Following affinity purification using anti-GFP nanobody beads and on-bead cleavage by TEV, Pks13 was run through a sizing column, which gave two peaks (Extended Data Fig. 1a). The protein in each peak was composed of Pks13 as seen on SDS–PAGE, and was predominantly dimeric Pks13 as shown by 'blue native'–PAGE (Extended Data Fig. 1b,c). Therefore, the higher molecular weight peak 1 resolved in size-exclusion chromatography is a larger multimer that readily dissociates into a dimer. Liquid chromatography with tandem mass spectrometry (LC–MS/MS) confirmed the protein identity with 78.1% sequence coverage throughout the entire Pks13 (Extended Data Fig. 1d).

Cryogenic-electron microscopy (cryo-EM) was used to collect images of particles from the peak 1 fraction, which behaved better when frozen on grids compared to particles from peak 2 (Table 1). We added a benzofuran inhibitor of the terminal TE domain[17] 'TAM16' to part of the material, with the aim of stalling the throughput of the overall reaction and producing a more homogeneous stable structure. Samples with and without this inhibitor produced the same structures with marginally better resolution for the sample with inhibitor. We report data from the sample with the inhibitor. Material from the peak 1 fraction, when imaged by cryo-EM, revealed multiple conformational states of the protein. Image classification and refinement revealed a well-resolved, two-fold symmetric core comprising the KS, AT and parts of KS-AT linker domains (Figs. 2a and 3a and Table 1). Symmetry expansion and focused classifications were used to resolve the regions N terminal to the KS-AT didomain core, including the two alternative ACP1 domain

Fig. 1 | Overall architecture of the mycobacterial Pks13 showing two alternative positions of the ACP1 domain. a, Part of the *Ms* operon containing the *fadD32-pks13-accD4* locus (top). Pks13 is composed of 1,816 amino acids with seven domains, and five domains of recognized function with lengths shown to scale in sequence. Colors are preserved throughout the figures. An N-terminal acyl ACP1 (yellow) is followed by an aspartate glutamate-rich linker (DE-rich linker), KS (red), a KS-AT linker domain (navy blue), an AT (blue), AT-ACP2 linker (teal), ACP2 (green), a linker (gray), ACP3 (light purple) and TE (purple). ACP1 and ACP2 have the –DSL– motif that gets phosphopantetheinylated to receive substrate. The C terminus of Pks13 was tagged with a TEV-cleavable eGFP. **b**, Schematic of the Pks13 reaction. The meromycolyl substrate is attached to the Ppant arm (bold wavy line) of the N-terminal ACP (ACP1). This is followed by *trans*-thioesterification to the KS. The second substrate is attached to the active site serine of AT and then transferred to ACP2 for the decarboxylative Claisen condensation. The α-alkyl β-ketoacyl thioester product is released from ACP2 by the TE that ligates it to trehalose. CmrA reduces the product to yield TMM. **c**, A composite structure of the Pks13 homodimer showing the relative positions of ACP1a and ACP1b fitted into a composite cryo-EM map constructed from the focused reconstructions. The two protomers are distinguished from each other by darker shades of domain colors for one protomer, and lighter shades of the same color for the other. Domains in the lighter-colored protomer are labeled with the prime (′) designation. The left ELBOW region connects the lighter-colored KS and KS-AT linker domains. The right ELBOW connects the darker colored domains. The ELBOW and HINGE regions' resolutions (roughly 20 Å) indicate flexibility. **d**, The two positions of ACP1 (ACP1a and ACP1b) are followed by acidic residues in the DE-rich linker (yellow) that lie near basic residues on the KS (surface highlighted blue). Ppant attached to S38 is visible in ACP1a and labeled.

https://doi.org/10.1038/s41594-022-00918-0

structures (Figs. 2b and 3a,c and Table 1). There are also two lobes of density we term the ELBOW that connect the C-terminal end of the KS domain (E529) and the beginning of a well-resolved KS-AT linker domain (T588) (Fig. 1c). There is additional density above the KS dimer, which we term the HINGE region (Fig. 1c), indicating flexibility and dynamic motion of regions C terminal to the AT domain.

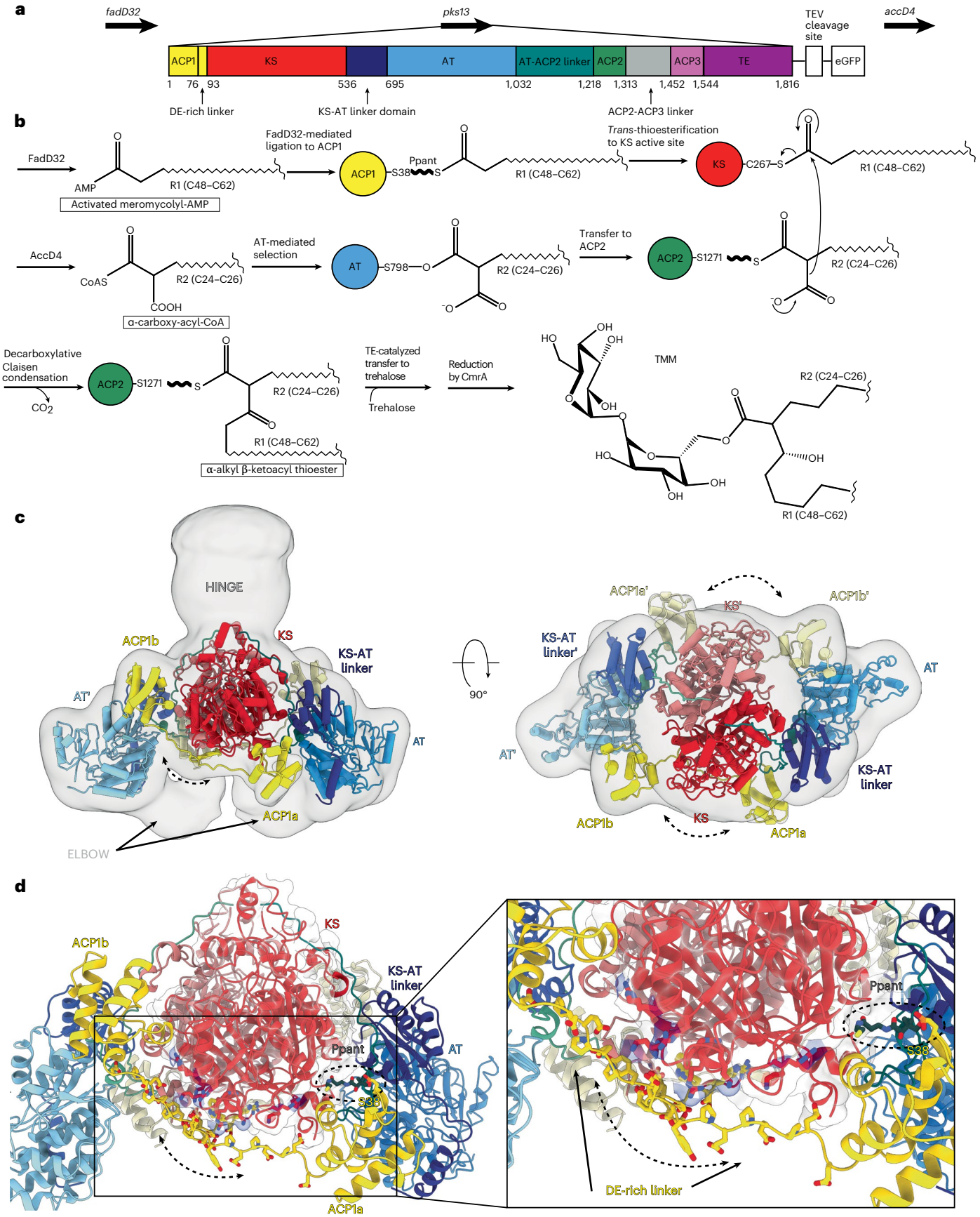

https://doi.org/10.1038/s41594-022-00918-0

Table 1 | Cryo-EM data collection, refinement and validation statistics

	KS-AT consensus refinement, EMD-26574, PDB 7UK4	ACP1a-KS-AT, EMD-27002, PDB 8CUY	ACP1b-KS-AT, EMD-27005, PDB 8CV1	KS-AT$_{in}$, EMD-27003, PDB 8CUZ	KS-AT$_{out}$, EMD-27004 PDB 8CV0
Data collection and processing					
Magnification					
Voltage (kV)	300	300	300	300	300
Electron exposure (e$^-$/Å^2)	67	67	67	67	67
Defocus range (μm)	0.7–1.5	0.7–1.5	0.7–1.5	0.7–1.5	0.7–1.5
Pixel size (Å)	0.4175	0.4175	0.4175	0.4175	0.4175
Symmetry imposed	C2	C1	C1	C1	C1
Initial particle images (no.)	4,400,000	1,200,000	1,200,000	1,200,000	1,200,000
Final particle images (no.)	1,200,000	146,928	39,685	123,116	92,662
Map resolution (Å)	1.94	2.4	2.6	3.0	3.1
FSC threshold	0.143	0.143	0.143	0.143	0.143
Map resolution range (Å)	1.9–3.7	2.4–4.2	2.7–4.3	2.5–4.2	2.6–4.5
Refinement					
Initial model used (PDB code)	De novo	7UK4	7UK4	7UK4	7UK4
Model resolution (Å)	2.0	2.7	2.7	2.8	2.9
FSC threshold	0.5	0.5	0.5	0.5	0.5
Map sharpening *B* factor (Å^2)	-	48.65	9.79	-	-
Model composition					
Nonhydrogen atoms	14,487	14,917	14,771	14,084	14,084
Protein residues	1,856	1,944	1,939	1,850	1,850
Ligands	2	5	2	2	2
B factors (Å^2)					
Protein	45.1	109.8	82.2	41.0	41.5
Ligand	38.0	75.0	80.3	42.5	43.0
r.m.s. deviations					
Bond lengths (Å)	0.004	0.001	0.008	0.002	0.002
Bond angles (°)	0.584	0.360	0.673	0.576	0.562
Validation					
MolProbity score	1.21	1.21	1.50	1.49	1.39
Clashscore	2.57	4.31	5.50	2.83	3.08
Poor rotamers (%)	0.83	0.98	0.26	1.80	1.24
Ramachandran plot					
Favored (%)	97.08	98.55	96.79	96.57	96.63
Allowed (%)	2.92	1.45	3.06	3.43	3.37
Disallowed (%)	0.0	0.00	0.16	0.0	0.00

Meromycolyl substrates are bound to the KS dimer

The most ordered parts of the structures that include the KS, KS-AT linker and the AT domain were resolved to 1.8 Å atomic resolution from consensus C2 refinement and density modification (Fig. 2a). Pks13 is a parallel homodimer of the multidomain chains whose oligomerization is driven by the dimeric KS interface[18,19] (Fig. 1c). Substrate density protruding from each of the catalytic C267 residues in the KS dimer core (Fig. 4) extends 'upward' through a hydrophobic tunnel labeled 'KS lipid conduit' that reaches the solvent. Covalently bound fatty acid chains were identified by base hydrolysis and mass spectrometry (Methods). Following identification of the attached chains we determined that the meromycolate branch of chains attached to C267 are one of either the α_2 mycolic acid ($C_{55}H_{106}O_2$), **10**, or the α' mycolic acid ($C_{40}H_{78}O_2$), **11** (ref. [20]) (below). These two alternative chains were previously activated by FadD32 AMPylation, and transferred onto the thiol of the Ppant arm attached to S38 of ACP1 with release of AMP[21] (Fig. 1b), and subsequently translocated into the KS active site by *trans*-thioesterification (Fig. 1b).

Multiple ordered water molecules are seen within hydrogen-bonding distances of the conserved KS catalytic triad C267, H403 and H443 (refs. [10–12,18,22]) (Fig. 4a). The atomic structure of the active center and the positions of the first 18 CH_2 groups of the substrate acyl chain are well defined by the density at 2.4 Å resolution (determined using *Q* scores)[23] (Figs. 3b and 4c). The distal parts of these chains reside outside the KS domain and are not visible in density indicating that they are less well ordered. They may possibly be sequestered by the detergent in our preparation.

ACP1 is seen in two alternative positions

Two stable positions of the ACP1 (ACP1a and ACP1b) with respect to the KS-AT dimeric structure were resolved using symmetry expansion and focused classification (Fig. 2b and Supplementary Video 1). The ACP1a-KS-AT and ACP1b-KS-AT reconstructions are superimposed as a composite density map to display their relative positions (Fig. 1c). The ACP1a-KS-AT reconstruction was refined to 2.4 Å, and the ACP1b-KS-AT reconstruction was refined to 2.6 Å by gold standard Fourier shell correlation (GSFSC), with lower resolutions for the ACP1a and ACP1b (3.6 and 4.6 Å, respectively, from map-to-model comparisons using *Q* scores[23]) (Figs. 2b and 3c).

ACP1a and ACP1b each have continuous density for residues 76–92 that connect ACP1 to the downstream KS. This 17-amino acid linking sequence (E76–R92) that we term the 'DE-rich linker' is negatively charged with nine acidic amino acids (E76, E78, E80, E82, D85, E86, D87, E88, D89). This linker adopts an extended chain configuration (Fig. 1c,d). The last six amino acids (D87–R92) from the ACP1a and ACP1b conformers closely overlap in position and are near a positively charged surface of the KS containing R282, R384 and K388 (Extended Data Figs. 2 and 3). Notably, E88 hydrogen bonds with R384 in the ACP1a conformer, and with R384 and K388 in the ACP1b conformer (Extended Data Figs. 4 and 5). The preceding sequence of 11 amino acids (E76–E86) lie near positively charged surface tracts of two different regions on the KS surface (Fig. 1d and Extended Data Figs. 2–5). These positively charged surfaces are in stark contrast to the otherwise predominantly negatively charged electrostatic surface of the KS (Extended Data Fig. 3).

The distance between ACP1a and ACP1b is approximately 60 Å with roughly 180° rotation of ACP1. ACP1a makes contacts with the KS, KS-AT linker domain, and the AT-ACP2 linker via its helix 2 and 3, and the 2–3 loop joining them (Extended Data Fig. 6). This position is not seen in other PKSs or fatty acid synthases. The total buried surface area of 1,106 Å^2 is consistent with it being a transient association (Fig. 1c,d and Extended Data Fig. 6)[24]. Analysis of the interface using PISA suggests that it is an unusually hydrophobic interface with a 'predicted solvation free energy' of formation $\Delta G^{\prime}$ of −8.5 kcal mol^{-1} (ref. [25]). There is a notable parallel, displaced pi-pi stacking interaction between guanidinium groups of R63 on the ACP1a and R496 on the KS (Extended Data Fig. 6). The displaced pi-pi stacking interaction between R63 of ACP1a and R496 of the KS domain is not uncommon. Indeed 3.6% of all arginine side chains recorded in the Protein Data Bank (PDB)[26] were found in this interaction with each other[27]. The parallel but displaced guanidinium groups are 4.0 Å apart and each is stabilized in its orientation by intra-domain hydrogen bonds or charge-charge interactions with nearby carboxyl groups within the same domain. The Arg interactions with the negatively charged carboxyl groups minimize the repulsive electrostatic energy between the stacked guanidinium groups[28]. These interactions add specificity to this ACP1a-KS-AT linker orientation. The Ppant arm attached to S38 of ACP1a is clearly resolved in density maps, and shows that it is not bound to a fatty acid chain (Extended Data Fig. 6).

The second ACP1 position, ACP1b, is much closer than ACP1a to the second branch of the KS hydrophobic tunnel that forms a putative 'lipid delivery conduit' into the KS active site (Fig. 4a,b). ACP1b contacts the KS from the same protomer with a total of 495 Å^2 buried surface area through a hydrophobic interface (Extended Data Fig. 7b). ACP1b also contacts the AT′ from the opposite protomer with a buried surface area of 126 Å^2. This interface is more hydrophilic than the interface with KS and includes polar residues (Extended Data Fig. 7a)[25]. S38 of ACP1b, which receives the Ppant arm, is 27 Å away from the KS active site C267 of the same protomer (Supplementary Fig. 2) where the meromycolyl substrate is seen attached in the structure. The Ppant arm seen in ACP1a is not resolved in the alternative ACP1b position due to limited resolution there, indicating that it is too flexible to be defined.

The negatively charged nature of the DE-rich linker is generally conserved although not the specific amino acid sequences themselves, and the positively charged surfaces are conserved among Pks13 homologs from other mycobacterial species (Supplementary Fig. 3). This suggests a role of this linker and its interactions in guiding the dynamic trajectory of ACP1 for meromycolate delivery from FadD32 to the active site of the KS domain.

The number of particles seen on the EM grids is roughly 3–4 times higher for ACP1a than for ACP1b indicating a very small energy difference between the two states. Applying the free energy relationship between two states b and a at equilibrium, $\Delta G^0 = RT\ln([b]/[a])$ of roughly 0.8 kcal mol^{-1} suggests a very small difference in free energy between these two states. This distribution is consistent with ACP1 function in readily accessing these positions to facilitate forward translocation of the meromycolyl chain.

The AT domain bound to the α-branch substrate

The second shorter 'α-branch' substrate chain (the α-carboxy-acyl-CoA (R2 C_{24}–C_{26})), which is carboxylated by AccD4, gets transacylated from CoA to the active site serine (S798) of the AT domain to form an ester[29] (Fig. 1b). A clear density for the covalently bound α-carboxy substrate was observed at S798 at the AT active site in the ACP1a conformer. The endogenous substrate was resolved at 3.2 and 3.7 Å resolution (determined using *Q* scores) in each protomer, and is visible for the first eight carbons of the acyl chain (Extended Data Fig. 8). This proximal end of the substrate occupies a hydrophobic tunnel we term the 'AT lipid conduit' (Fig. 5a). This chain is analogous to the 'extender unit' of modular PKSs[10,30] (Fig. 1b and Supplementary Fig. 1). The α-carboxy-acyl chain is subsequently transferred from the AT to the Ppant arm thiol bound to S1271 of the downstream ACP2. From there the R2-bound ACP2 is inserted into the KS active site to undergo decarboxylative Claisen condensation with the meromycolyl-cysteine adduct at C267 (Fig. 4a). Decarboxylative condensation results in the α-alkyl β-ketoacyl thioester product, the direct precursor of mycolic acid[9] (Fig. 1b and Supplementary Fig. 1). The R stereochemistry at position 2 that bears the carboxyanion is conserved in all mycolic acids showing that the Pks13 reaction is stereospecific[13].

The native α-carboxylated substrate of the AT domain lies in a cleft between the α/β hydrolase and ferredoxin-like subdomains of the AT (Fig. 5a, Extended Data Fig. 8 and Supplementary Video 1). The carboxylate of the carboxy-acyl serine ester intermediate is stacked against the face of the phenyl ring of F709 (Fig. 5a and Extended Data Fig. 8). F709 in turn makes an edge to face pi stacking interaction with F899. This type of anion-pi-pi stacking has been observed in many protein structures[31]. There is a pi-cation interaction between F899 and

Fig. 2 | Single-particle analysis processing workflow from videos through consensus C2 refinement and focused refinements. a, Image processing workflow done in cryoSPARC for the initial consensus C2 refinement. Particle image pose heat map (displayed as blue to red, low to high numbers of images) showing an isotropic distribution, complete GSFSC plots using the $FSC_{0.143}$ criterion and the local resolution map are shown. CTF, contrast transfer function. **b**, Symmetry expansion and focused classification done in RELION probing ACP1 and AT domain dynamics. Two classes were seen for positions of the ACP1, namely, ACP1a (blue) and ACP1b (blue). Local resolution maps for the ACP1a and ACP1b structures illustrating lower resolution for the ACP domain are shown. The number of particles is roughly 3 to 4 times higher for ACP1a than for ACP1b indicating that if these represent similar proportions in solution, there is a very small energy difference between the two states. Two conformations of the AT domain (blue region in both) were identified and used for focused refinement. The soft masks used for focused classification encompass the blue-colored regions of each map, each dilated roughly 10 Å around the regions of interest. The maps showing the blue-colored regions are viewed down the pseudo-symmetry axis, orthogonal to the viewing direction in **a**. For each focused refinement, GSFSC plot using the $FSC_{0.143}$ criterion is shown.

https://doi.org/10.1038/s41594-022-00918-0

R897, which may serve to polarize the aromatic rings sufficiently to stabilize the carboxylate-F709 interaction. The Nε of the catalytic base H906 is close to both the Oγ of S798 (4.3 Å) and to the carbonyl oxygen of the substrate ester (3.9 Å), supporting its action as both the catalytic base and as a stabilizing force for the carbonyl oxyanion intermediate during the reaction. The imidazole of H906 is pinioned by hydrogen

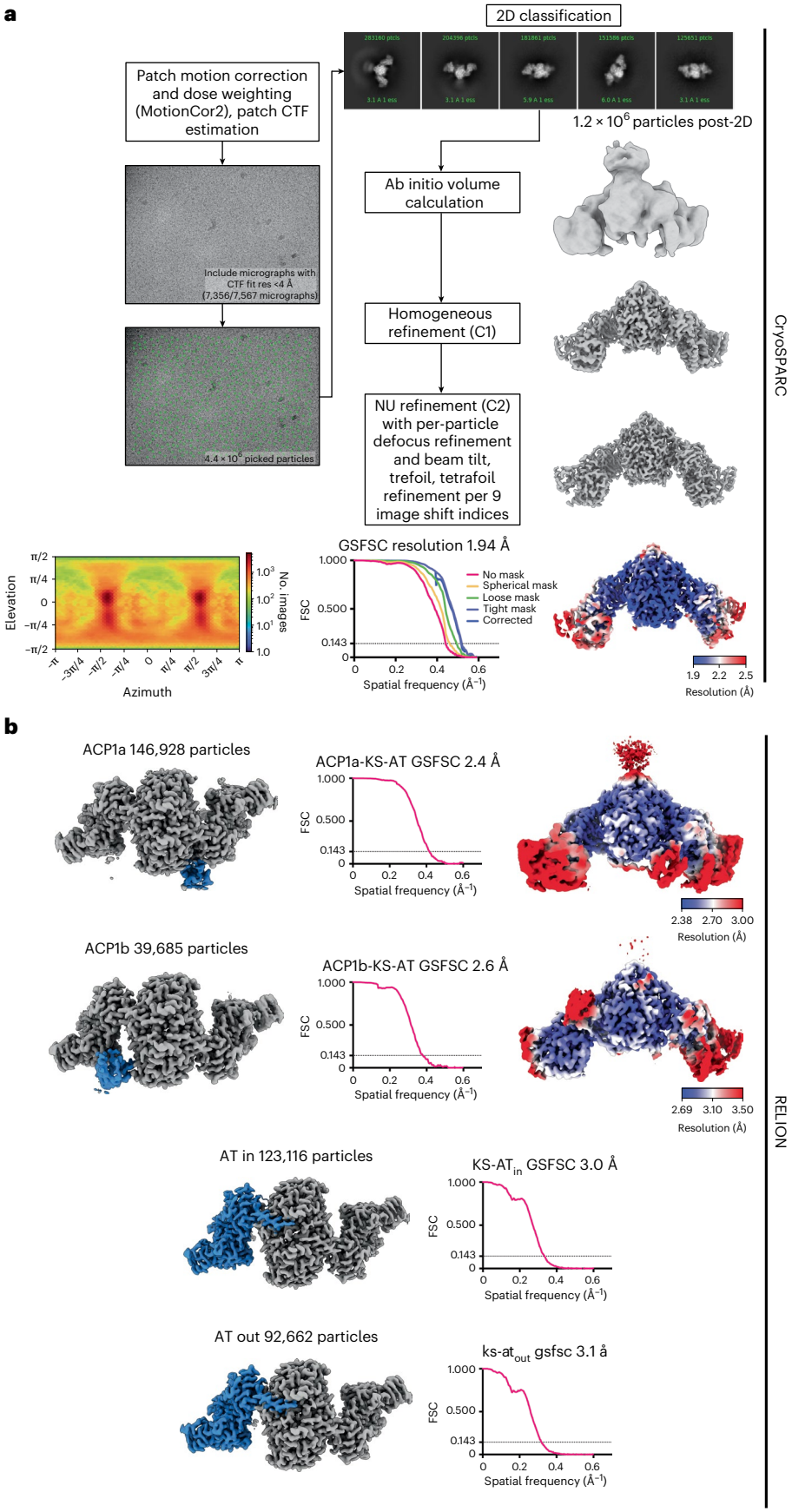

https://doi.org/10.1038/s41594-022-00918-0

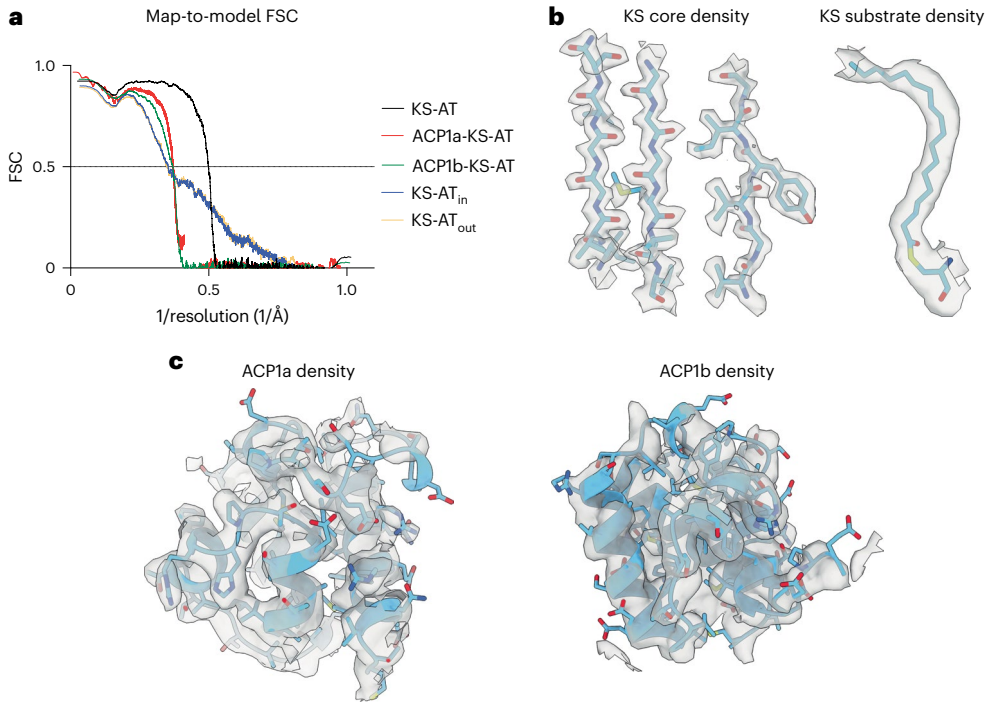

Fig. 3 | Map-to-model FSCs, and example EM densities. a, Map-to-model FSC curves for all the structures described from consensus refinement and focused classifications and refinements. **b**, Near-atomic resolution density in the KS core. Beta strands are shown (left) and lipid density extending upward from the KS active center C267 (right). **c**, Density for ACP1a (left) and ACP1b (right).

bonds from the $N_{\delta 1}$-H to the carbonyl oxygens of G959 and H962. The Nε of H906, Oγ of S905 and NH_2 of the R823 guanidinium group are all oriented to stabilize the oxyanion formed during the catalytic reaction (Extended Data Fig. 8b).

When compared with the structure of a 52 kDa AT-containing fragment of *Mtb* H37Rv (ref. [29]) in complex with an α-carboxy palmitoyl substrate mimetic, our *Ms* Pks13AT has a root mean squared (r.m.s.) deviation of 1.00 Å versus the fragment; however, the long fatty acid substrate density lies in a different solvent-exposed hydrophobic tunnel ('lipid conduit' in Fig. 5a, Supplementary Fig. 4 and Supplementary Video 1), and the Pks13 active site differs in that the guanidinium cation of R823 (R826 in *Mtb*) does not form a bidentate salt bridge with the α-carboxy group of the substrate fatty acid but is a key part of the oxyanion binding site formed during the reactions. These differences between the isolated AT and our multidomain structures may reflect conformational restraints introduced by interactions of the AT domain with the KS and ACP1 domains in the native Pks13 environment. Such restraints may modulate access for substrate translocation to the ACP2.

KS and AT domains are connected by a flexible ELBOW that incorporates 59 unmodeled amino acids between residues 529 and 588 with its general location defined in the density (Fig. 1c and Supplementary Fig. 5). An amphipathic helix (residues 588–608) found only in mycobacterial Pks13s leads into the well-ordered KS-AT linker domain (Supplementary Fig. 5). After symmetry expansion and focused classification, two discrete alternative conformations of the AT domain relative to the KS domain were resolved (Fig. 2b). The two positions of each AT are rotated by 7° relative to the KS-AT linker domain (Fig. 5b and Supplementary Video 1). This change cannot yet be correlated with any particular functional role in Pks13. The AT-ACP2 linker (residues 1,032–1,074) is well defined as an extended chain along the surface of the KS domain. It remains possible that this AT conformational change may accompany repositioning of some of the other domains that are C terminal to the AT-ACP2 linker.

C-terminal regions are outlined by low resolution densities

The 'HINGE' region (Fig. 1c) and two lenticular densities 'on top' of the two-fold axis of the KS-AT domains (Fig. 6) account for some or all of the remaining domains of the structure: these domains comprise a 143 amino acid linker (1,075–1,217), ACP2, a 138 amino acid linker, ACP3 and the TE domain (Fig. 6a,b). These two density maps were recovered from symmetry expansion and focused classification with a large radius mask and were resolved at low (roughly 20 Å) resolution. Because the densities seem to connect these two classes at low contour levels, we suggest that the structure may rock about the AT-ACP2 linker to HINGE connection by roughly 40° between these two states on either side of the dimeric core. This indicates flexibility around the HINGE region to allow this movement in transferring substrates between the domains, and may account for the lower resolution in these regions. This kind of flexibility is consistent with the need for the ACP2 to pick up the α-carboxy-acyl chain from the active center of an AT domain, then transport it for condensation with the meromycolyl chain on a KS domain, and to then transport the then two-chain α-alkyl β-ketoacyl thioester to the TE domain for transfer to trehalose. Solution structures of Pks13 also indicate flexibility between the N-terminal regions, including the ACP-KS-AT domains and the ACP2-TE domains[32].

Identification of the bound substrate chains

The proximal regions of substrates at the active sites of the KS and AT domains are well defined in the density at 2.4 and 3.2 Å resolution. Density for the distal parts is more diffuse, consistent with less specific binding of the aliphatic chains outside the tunnels. The substrates attached to Pks13 were identified by hydrolysis followed by normal phase LC coupled with electrospray ionization (ESI)–high-resolution mass spectrometry. Their predicted and observed mass-to-charge ratios (*m/z*) accurate to three decimal places are listed in Supplementary Table 1. Three very long-chain fatty acids series were identified: (1) the longest series is centered around $C_{55}H_{106}O_2$ **12** with exact mass of 798.819 Da (Supplementary Fig. 6) and corresponds to R1 (Fig. 1b).

https://doi.org/10.1038/s41594-022-00918-0

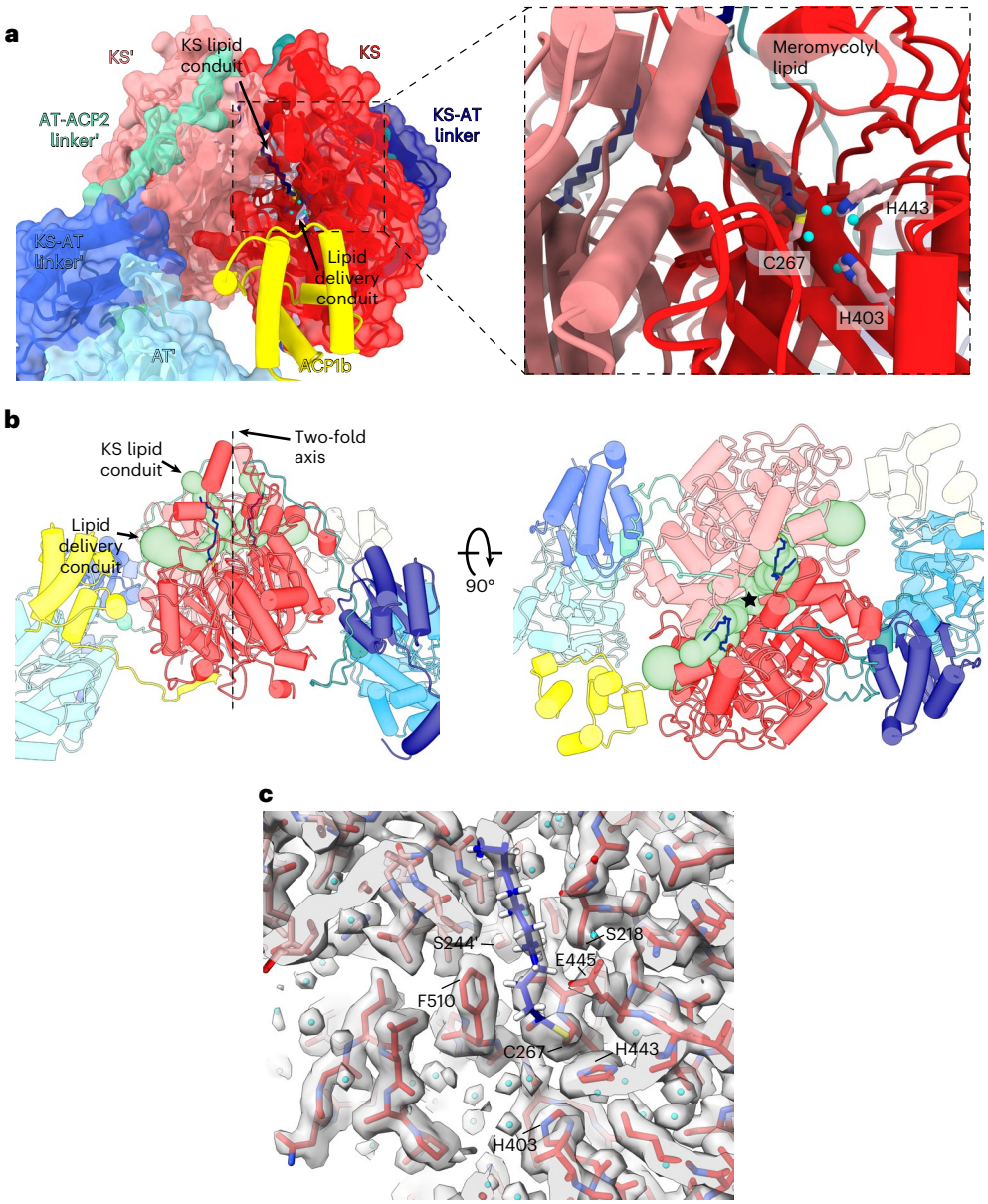

Fig. 4 | Meromycolyl substrate in the KS active site. a, A view of the ACP1b (yellow) near the KS (red) of the same protomer near the putative lipid delivery conduit. The inset shows a close up view of the KS active site. The meromycolyl substrate is a thioester adduct with C267 and density for the lipid is shown within 2 Å about the carbon atoms. Active site residues C267, H443 and H403 involved in *trans*-thioesterification are shown in pink. Water molecules within hydrogen-bonding distance of active site residues are shown as cyan spheres. **b**, Front (left) and top (right) views of the ACP1b conformer structure with two branches of a hydrophobic tunnel (KS lipid conduit and lipid delivery conduit) shown as green surface models. The approximate location of the two-fold axis is indicated as a dotted line and labeled in the front view (left) and by a star in the top view (right). **c**, Density for the catalytic site and surrounding regions and water molecules, and the proximal portion of the meromycolyl substrate attached to C267.

It is consistent with being the 'alpha-2' meromycolate branch (C_{51}–C_{57}) found in *Ms*[33,34], seen attached to C267 of the KS structure (Fig. 4). (2) A series centered around $C_{40}H_{78}O_2$, **13** with an exact mass of 590.600 Da (Supplementary Fig. 7) corresponds to an alternative R1, and is termed the 'alpha-prime' meromycolate branch of length C_{36}–C_{42} with C_{40} being most represented. This chain is consistent with the meromycolate branch of α' mycolic acid found in *Ms* but not found in *Mtb*. (3) A series centered around $C_{24}H_{48}O_2$, **14** with exact mass 368.365 Da (Supplementary Fig. 8) corresponds to R2, a C_{22}–C_{26} fully saturated chain with C_{24} as most represented (termed lignoceric acid) (Fig. 1b). This fatty acid is consistent with the α-carboxy-acyl chain attached to the AT active site as seen in the density (Fig. 5a and Extended Data Fig. 8). The mass, however, indicates that it lacks the expected α-carboxyl group that is seen in the density map. The carboxyl group may have been released during the hydrolysis from Pks13, or during mass spectrometry. The residue-specific attachment sites of fatty acids to the peptide chain, previously established for *Mtb*[10], were not further reverified experimentally due to the difficulty of obtaining mass spectra of these long-chain fatty acids attached to peptides.

Proximity of domain locations and integrative modeling

The diffuse densities for regions of Pks13 that are C terminal to the AT-ACP2 linker in linear sequence suggest structural flexibility and a heterogeneous localization of these domains, as required to transfer substrates. To determine the localization of the flexible domains in solution, we performed cross-linking mass spectrometry (XL–MS). We

https://doi.org/10.1038/s41594-022-00918-0

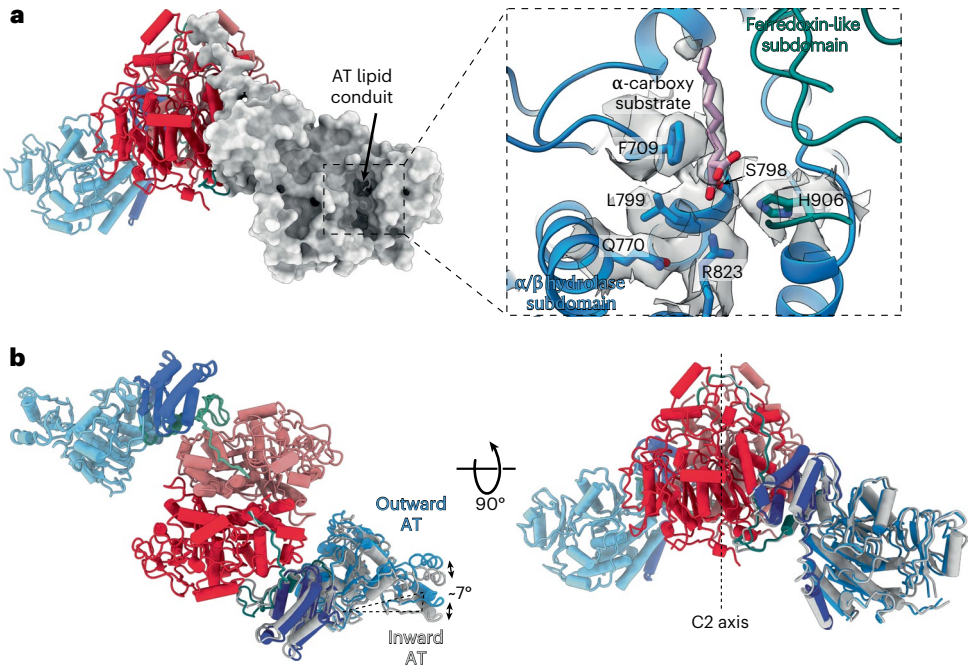

Fig. 5 | Substrate-bound AT active site, and alternative inward and outward positions of the AT domain. a, Cartoon and surface representations viewed perpendicular to the vertical two-fold axis showing the lipid conduit in the AT domain. The inset shows an expanded view of the density for the α-carboxy lipid substrate in the AT lipid conduit between the α/β hydrolase subdomain (blue) and the ferredoxin-like subdomain (dark cyan). The α-carboxy substrate is attached as an ester linkage at S798. Surrounding active site residues, including the catalytic base H906, are labeled and shown with corresponding density. Density and atomic structure for the entire region is shown in stereo in Extended Data Fig. 8. **b**, Overlay of the AT conformers show the AT movement roughly 7° outward from their hinge point at the KS-AT linker domain. The inward conformation is shown in gray. Hinge movement is elaborated in Supplementary Video 1.

used a disuccinimidyl sulfoxide (DSSO, **14**)-based XL–MS^3 approach[35,36] (Methods). The spacer arm that bridges linked residues is 10.3 Å in length. When estimating distances between α-carbons of inter-linked lysine amino groups or the N-terminal amine, we allowed for free-rotation, and therefore we classified a cross-link as satisfied if the Cα–Cα distance spanned by the cross-linked residues was less than 35 Å (ref. [37]).

We cross-linked natively purified Pks13 with increasing amounts of DSSO at 37 and at 4 °C (Supplementary Fig. 9). All bands associated with cross-linked products were excised from an SDS gel and analyzed by XL–MS^3 (Supplementary Fig. 9). After removing data files associated with highly cross-linked samples (Methods), we used the filtered XL–MS^3 dataset (Methods) and identified 604 redundant interlinks that corresponded to 57 unique linkages (Supplementary Table 2 and Supplementary Fig. 10c). To model the domains not seen in ACP1a or ACP1b configurations, and to capture flexibility in the in-solution structure, we used the 57 unique linkages (Extended Data Fig. 9) from the filtered XL–MS dataset for integrative modeling.

Lysine 677 forms several cross-links to other domains that are present in the protein sample but defined only as diffuse domains in the structure (Fig. 6), and the cross-links then support that the ACP2, ACP3 and the TE domain come close to the AT domain. This is necessary for the ACP2 to transport the α-chain from the AT domain to the KS active site to evoke the final condensation, and then to reach the TE domain for *trans*-esterification to trehalose. While most of the 33 cross-links formed within the atomistic portions of the Pks13 dimer structure are consistent with known distances in the dimeric structure, several are too far apart (Supplementary Fig. 10d and Supplementary Tables 2 and 3). These are consistent with unexpected flexibility within the structure or higher order assemblies of Pks13 dimers as indicated in the dimer of dimers seen as peak 1 in the size-exclusion profile (Extended Data Fig. 1a).

A structural model of the Pks13 dimer was computed by integrative modeling[38–42] based on the 57 chemical interlinks (Extended Data Fig. 9 and Supplementary Tables 2 and 3) and structural models of the components of the Pks13 dimer (Supplementary Table 4). These components include the current atomic structural model based on the cryo-EM maps, de novo AlphaFold2 predictions of domains unresolved in the cryo-EM structure[43,44] and flexible linker regions. The cross-links were obtained from populations of structurally dynamic protein complexes as they exist in solution. A model of the Pks13 dimer was computed by satisfying this input information to the best possible degree using Integrative Modeling Platform[45]. The resulting ensemble of acceptable models satisfies 91% of the cross-links (Extended Data Fig. 10a,b,c and Fig. 6c). The unsatisfied (over 35 Å) cross-links span mostly residues in the KS and AT domains, indicating that the rigid representation of the system is not adequate to capture the full range of conformations in solution. The integrative structure localizes the AT-ACP2 linker and ACP2 domain to the 'HINGE' region of the cryo-EM density map and suggests large uncertainty in the configuration of the ACP3 and TE domains within an arch-like volume above the 'HINGE' (Fig. 6) or around the KS and AT domains (Extended Data Fig. 10a). This uncertainty can in principle arise from both the actual structural dynamics of the domains, and relative lack of input information; it is difficult to deconvolute the two possibilities. Furthermore, the model indicates that the distances between the active sites of the ACP1(S38)-KS(C267), AT(S798)-ACP2(S1271), KS(C267)-ACP2(S1271) and ACP2(S1271)-TE(S1616) domains are highly variable, but that these active sites come into proximity (Extended Data Fig. 10d).

Discussion

A cartoon of the chemical scheme deduced from the structural arrangement is shown in Fig. 7. The overall structure of Pks13 is a dimeric assembly of a series of domains that operate in ordered sequence between domains to assemble mycolic acids by condensation of two long-chain fatty acids. These unusually long-chain reactants are moved by carrier proteins (ACPs) between domains of the dimer. Within the dimer,

https://doi.org/10.1038/s41594-022-00918-0

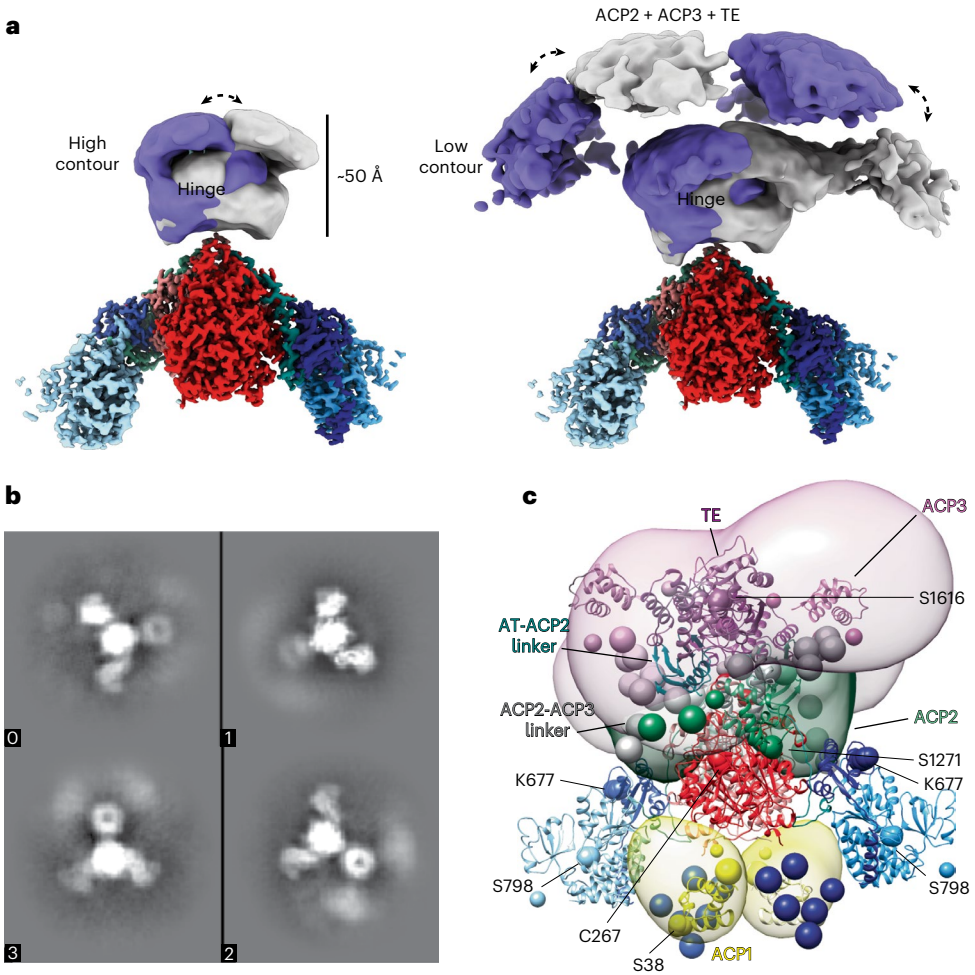

Fig. 6 | C-terminal domains are visualized at low resolution in two alternative positions. a, The HINGE and C-terminal domains are visible at roughly 20 Å resolution in the cryo-EM map above the KS-AT domains. Using a large radius mask two conformations of the HINGE and C-terminal domain densities were recovered from focused 3D classification, shown in purple and gray, respectively. Hence each of these image classes represent an asymmetric structure with respect to the two-fold symmetric high-resolution components. These two asymmetric states include the HINGE region and have low diffuse density between them indicating rocking between these alternative states. There is higher density in the HINGE region (left), versus the lenticular densities (right). **b**, 2D classes showing smeared density attributed to the AT-ACP2 linker, ACP2, ACP2-ACP3 linker domain, ACP3 and TE domains that have multiple positions around the connection to the AT domains at the base of the HINGE. **c**, Integrative structure model of the Pks13 dimer based on the cryo-EM structure, chemical cross-linking and AlphaFold2 predictions. The model represents the centroid of the ensemble of good scoring models obtained through Monte Carlo sampling. Regions with well-defined structures were modeled as rigid bodies (shown as ribbons), while regions with no available structure or flexible regions were represented as strings of beads corresponding to up to ten residues per bead (shown as beads). The structural ensemble is presented as a 3D localization probability density whose surface is rendered transparent for visual clarity, using the same color scheme for domains as in Fig. 1a. Complete analysis of all classes is shown in Extended Data Fig. 10. Two-fold symmetry was applied to compute the model. Key residues, including K677 and active site residues S38, C267, S798, S1271 and S1616 are shown as spheres.

domains from the two protomers are arranged across the two-fold axis, and by their relative proximities can operate sequentially on the substrates in *cis* or in *trans* between domains on either protomer of the dimer. The catalytic functions of several isolated domains of PKSs have been described independently at the levels of atomic structure and reaction chemistry[18,46–49] although not previously seen in the context of their native environment.

The alternative ACP1 positions

Since both ACP1a and ACP1b are well-ordered structures with specific hydrophobic interfaces, we suggest that these may be intermediate positions on the pathway to deliver the meromycolate branch to the KS active site via the delivery conduit. The absence of clear density for the incoming meromycolate on the Ppant of ACP1a suggests that the structure is of an intermediate state following delivery of the R1 chain to the KS active site, and preceding the next FadD32 catalyzed attachment of the acyl-adenylate intermediate to the Ppant on the S38 of the ACP1a (ref. [12]). The meromycolyl substrates in the KS active site and the lack of the meromycolate density on the S38 of ACP1b suggest that this structure may represent the postdelivery position of the ACP1 retreating from the loaded KS domain. A conserved active site loop in KS is proposed to be a gate that opens to accept substrate[50]. In Pks13, this loop is in a closed position, consistent with the structure we determine being in a postdelivery state.

The serine S38 attached to the Ppant arm is removed roughly 17 Å from the position required to deliver the meromycolate (Supplementary Fig. 11a). A twist of ACP1b about its connection to the N-terminal end of the DE-rich linker would position ACP1 S38 approximately 19 Å, the approximate length of the Ppant arm, from C267 of KS, allowing the Ppant thioester to deliver substrate to the KS active site (Supplementary Fig. 11a). In this docked position, helix III of ACP1 interacts with the KS accepting substrate, and loop 1 interacts with the KS′, KS-AT

https://doi.org/10.1038/s41594-022-00918-0

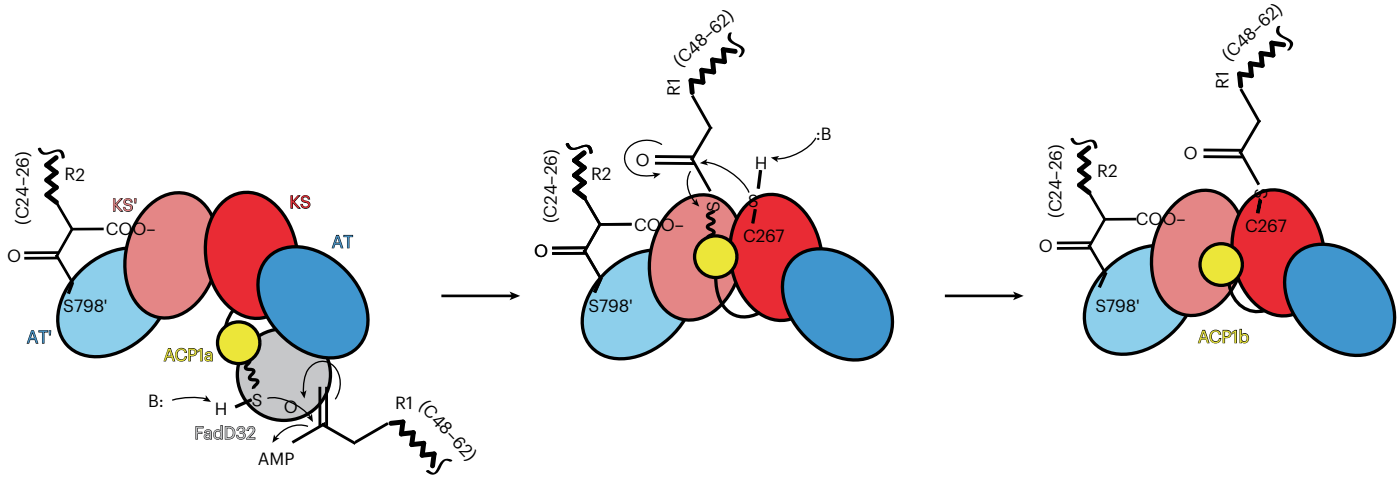

Fig. 7 | Proposed pathway to the structures determined for substrates bound Pks13. The chemical changes during the mechanism of Pks13 are schematized for just one side of the two-fold symmetric Pks13 dimer for clarity, and incorporating the two structures (ACP1a, ACP1b) we determined. The steps may occur in *trans* between alternative protomers as suggested by the relative proximities of the active sites of KS and AT of the contralateral protomer. Only the ACP1a, ACP1b, KS and AT domains are cartooned to describe this initial part of the reaction up to the structure we determined (third panel). The left panel shows an early stage of the catalytic cycle in which the R2 fatty acid substrate chain of length $(CH_2)_{24-26}$ is attached to the AT domain as seen in the structure (Fig. 5a). The Ppant arm depicted as a wavy line ending in a sulfhydryl and seen on ACP1a (yellow, first panel) links to the adenylated meromycolyl substrate (R1 $(CH_2)_{48-62}$) from FadD32. ACP1 delivers the attached meromycolyl substrate to the KS active site C267 through *trans*-thioesterification as seen in the structure (third panel). This is the stable state reflected in the structure with native substrates bound. In the subsequent steps (not shown; schematized in Supplementary Fig. 1b) the carboxy-acyl substrate R2 is transferred to ACP2. Decarboxylative Claisen condensation proceeds between R1 and R2 where the enolate generated by decarboxylation attacks the meromycolyl thioester bound to the KS producing an α-alkyl β-ketothioester. Finally, the TE domain passes the condensed α-alkyl β-ketothioester product to trehalose and is released from Pks13. The product is subsequently reduced by CmrA to form TMM. TMM is subsequently transported across the plasma membrane by the transporter MmpL3 (ref. [13]).

linker′ and AT′ domains of the opposite protomer. The docked ACP1b orientation in Pks13 is rotated roughly 90° from the DEBS module 1 ACP binding mode (Supplementary Fig. 11b).

The KS delivery conduit observed in the Pks13 structure near the ACP1b position is the same tunnel where both *trans*- and *cis*-acting ACPs bind to their cognate KSs, but the ACP interfaces with the conduit are not conserved. Detailed comparisons of the other KS-AT structures and ACP binding modes are in the Supplementary Information and figures.

Bound substrates

The fatty acid chains we identified for R1 and R2 are as expected for covalent adducts in the reaction of Pks13 domains, at a particular state in the reaction. The mass associated with each fatty acid chain defines the chemistry without ambiguity. The mass of the R1 'alpha-2' $C_{55}H_{106}O_2$ species that is added to C267 indicates an unsaturated C=C double bond with an adjacent methyl substituent[33]. The alternative R1, 'alpha-prime' mycolate, contains an unsaturated cis double bond and is found in *Ms* (although not in *Mtb*)[20,34].

The requirement for detergent to release Pks13, we presume from the membrane, raises the question as to where the membrane association is encoded. We surmise that the very hydrophobic meromycolate chains might be chaperoned in part by the lipid bilayer, and so might provide the link that anchors Pks13 to the plasma membrane during mycolic acid synthesis.

Use of TAM16 as inhibitor of TE domain

The intent of using a TE inhibitor was to stall the throughput to final product, and thereby to make the sample more homogeneous structurally. The structure reported here is that of the TE-inhibited species that had a marginally better quality. However, the structure was also determined from the noninhibited sample. Both structures were otherwise indistinguishable, which argues that the substrate-bound states of KS and AT are stable states that do not proceed to the Claisen condensation in isolated Pks13 without some other input. Conceivably the reaction could be driven forward by the arrival of new substrates from FadD32, and AccD4, for example.

The synthesis of mycolic acids from very long-chain hydrophobic intermediates depends on a chaperoned pathway, in which Pks13 provides a means to control and react on three specific very long-chain fatty acids. In mycobacteria, the acyl-AMP ligase FadD32 and carboxylase AccD4 are encoded within a gene cluster composed of *fadD32-pks13-accD4*, consistent with their concerted role in the condensation process (Fig. 1a). This locus is found exclusively among the mycolic acid producing mycobacteria, and Corynebacterineae with high sequence identity. All three proteins are essential to *Mtb* and therefore are high value drug targets[9,51].

First-line antimycobacterials against *Mtb* target earlier portions of the mycolic acid synthetic pathway, consistent with the essential role of mycolic acid synthesis in *Mtb*. Strategies to inhibit the active sites of the ACPs, KS, AT, TE and the MmpL3 transporter of mycolic acids[52,53] have been proposed but not yet led to drugs. The structure of the dimeric Pks13 may add new prospects for antimycobacterial drug discovery that take advantage of those interfaces between domains that we do see change throughout the carrier protein-mediated transport of substrates. These structures also serve to lay the groundwork for further understanding the process of how long-chain fatty acids are translocated from their synthases to the Claisen condensation that results in mycolic acid synthesis.

Online content

Any methods, additional references, Nature Portfolio reporting summaries, source data, extended data, supplementary information, acknowledgements, peer review information; details of author contributions and competing interests; and statements of data and code availability are available at https://doi.org/10.1038/s41594-022-00918-0.

References

1. *Global Tuberculosis Report 2021* (World Health Organization, 2021).
2. Zuber, B. et al. Direct visualization of the outer membrane of mycobacteria and corynebacteria in their native state. *J. Bacteriol.* **190**, 5672–5680 (2008).
3. Hoffmann, C., Leis, A., Niederweis, M., Plitzko, J. M. & Engelhardt, H. Disclosure of the mycobacterial outer membrane: cryo-electron tomography and vitreous sections reveal the lipid bilayer structure. *Proc. Natl Acad. Sci. USA* **105**, 3963–3967 (2008).
4. Sani, M. et al. Direct visualization by cryo-EM of the mycobacterial capsular layer: a labile structure containing ESX-1-secreted proteins. *PLoS Pathog.* **6**, e1000794 (2010).
5. Grzegorzewicz, A. E. et al. Inhibition of mycolic acid transport across the *Mycobacterium tuberculosis* plasma membrane. *Nat. Chem. Biol.* **8**, 334–341 (2012).
6. Harding, E. WHO global progress report on tuberculosis elimination. *Lancet Respir. Med.* **8**, 19 (2020).
7. Ioerger, T. R. et al. Identification of new drug targets and resistance mechanisms in *Mycobacterium tuberculosis*. *PLoS ONE* **8**, e75245 (2013).
8. Sacchettini, J. C., Rubin, E. J. & Freundlich, J. S. Drugs versus bugs: in pursuit of the persistent predator *Mycobacterium tuberculosis*. *Nat. Rev. Microbiol.* **6**, 41–52 (2008).
9. Portevin, D. et al. A polyketide synthase catalyzes the last condensation step of mycolic acid biosynthesis in mycobacteria and related organisms. *Proc. Natl Acad. Sci. USA* **101**, 314–319 (2004).
10. Gavalda, S. et al. The Pks13/FadD32 crosstalk for the biosynthesis of mycolic acids in *Mycobacterium tuberculosis*. *J. Biol. Chem.* **284**, 19255–19264 (2009).
11. Trivedi, O. A. et al. Enzymic activation and transfer of fatty acids as acyl-adenylates in mycobacteria. *Nature* **428**, 441–445 (2004).
12. Léger, M. et al. The dual function of the *Mycobacterium tuberculosis* FadD32 required for mycolic acid biosynthesis. *Chem. Biol.* **16**, 510–519 (2009).
13. Marrakchi, H., Lanéelle, M.-A. & Daffé, M. Mycolic acids: structures, biosynthesis, and beyond. *Chem. Biol.* **21**, 67–85 (2014).
14. Herbst, D. A. et al. The structural organization of substrate loading in iterative polyketide synthases. *Nat. Chem. Biol.* **14**, 474–479 (2018).
15. Meniche, X. et al. Subpolar addition of new cell wall is directed by DivIVA in mycobacteria. *Proc. Natl Acad. Sci. USA* **111**, E3243–E3251 (2014).
16. Khosla, C. From active sites to machines: a challenge for enzyme chemists. *Isr. J. Chem.* **59**, 37–40 (2019).
17. Aggarwal, A. et al. Development of a novel lead that targets *M. tuberculosis* polyketide synthase 13. *Cell* **170**, 249–259.e25 (2017).
18. Pan, H. et al. Crystal structure of the priming beta-ketosynthase from the R1128 polyketide biosynthetic pathway. *Structure* **10**, 1559–1568 (2002).
19. Tang, Y., Kim, C.-Y., Mathews, I. I., Cane, D. E. & Khosla, C. The 2.7-Angstrom crystal structure of a 194-kDa homodimeric fragment of the 6-deoxyerythronolide B synthase. *Proc. Natl Acad. Sci. USA* **103**, 11124–11129 (2006).
20. Barry, C. E. et al. Mycolic acids: structure, biosynthesis and physiological functions. *Prog. Lipid Res.* **37**, 143–179 (1998).
21. Byers, D. M. & Gong, H. Acyl carrier protein: structure-function relationships in a conserved multifunctional protein family. *Biochem. Cell Biol.* **85**, 649–662 (2007).
22. Robbins, T., Kapilivsky, J., Cane, D. E. & Khosla, C. Roles of conserved active site residues in the ketosynthase domain of an assembly line polyketide synthase. *Biochemistry* **55**, 4476–4484 (2016).
23. Pintilie, G. et al. Measurement of atom resolvability in cryo-EM maps with Q-scores. *Nat. Methods* **17**, 328–334 (2020).
24. Klaus, M. et al. Protein-protein interactions, not substrate recognition, dominate the turnover of chimeric assembly line polyketide synthases. *J. Biol. Chem.* **291**, 16404–16415 (2016).
25. Krissinel, E. & Henrick, K. Inference of macromolecular assemblies from crystalline state. *J. Mol. Biol.* **372**, 774–797 (2007).
26. Berman, H. M. et al. The Protein Data Bank. *Nucleic Acids Res.* **28**, 235–242 (2000).
27. Vernon, R. M. et al. Pi-Pi contacts are an overlooked protein feature relevant to phase separation. *eLife* **7**, e31486 (2018).
28. Lee, D., Lee, J. & Seok, C. What stabilizes close arginine pairing in proteins? *Phys. Chem. Chem. Phys.* **15**, 5844–5853 (2013).
29. Bergeret, F. et al. Biochemical and structural study of the atypical acyltransferase domain from the mycobacterial polyketide synthase Pks13. *J. Biol. Chem.* **287**, 33675–33690 (2012).
30. Gande, R. et al. Acyl-CoA carboxylases (accD2 and accD3), together with a unique polyketide synthase (Cg-pks), are key to mycolic acid biosynthesis in Corynebacterianeae such as *Corynebacterium glutamicum* and *Mycobacterium tuberculosis*. *J. Biol. Chem.* **279**, 44847–44857 (2004).
31. Lucas, X., Bauzá, A., Frontera, A. & Quiñonero, D. A thorough anion-π interaction study in biomolecules: on the importance of cooperativity effects. *Chem. Sci.* **7**, 1038–1050 (2016).
32. Bon, C. et al. Solution structure of the type I polyketide synthase Pks13 from *Mycobacterium tuberculosis*. *BMC Biol.* **20**, 147 (2022).
33. George, K. M., Yuan, Y., Sherman, D. R. & Barry, C. E. The biosynthesis of cyclopropanated mycolic acids in *Mycobacterium tuberculosis*. Identification and functional analysis of CMAS-2. *J. Biol. Chem.* **270**, 27292–27298 (1995).
34. Yuan, Y. & Barry, C. E. A common mechanism for the biosynthesis of methoxy and cyclopropyl mycolic acids in Mycobacterium tuberculosis. *Proc. Natl Acad. Sci. USA* **93**, 12828–12833 (1996).
35. Piersimoni, L. & Sinz, A. Cross-linking/mass spectrometry at the crossroads. *Anal. Bioanal. Chem.* **412**, 5981–5987 (2020).
36. Kaake, R. M. et al. A new in vivo cross-linking mass spectrometry platform to define protein-protein interactions in living cells. *Mol. Cell Proteom.* **13**, 3533–3543 (2014).
37. Merkley, E. D. et al. Distance restraints from crosslinking mass spectrometry: mining a molecular dynamics simulation database to evaluate lysine-lysine distances. *Protein Sci.* **23**, 747–759 (2014).
38. Kaake, R. M. et al. Characterization of an A3G-VifHIV-1-CRL5-CBFβ structure using a cross-linking mass spectrometry pipeline for integrative modeling of host-pathogen complexes. *Mol. Cell Proteom.* **20**, 100132 (2021).
39. Sali, A. From integrative structural biology to cell biology. *J. Biol. Chem.* **296**, 100743 (2021).
40. Saltzberg, D. J. et al. Using Integrative Modeling Platform to compute, validate, and archive a model of a protein complex structure. *Protein Sci.* **30**, 250–261 (2021).
41. Saltzberg, D. et al. Modeling biological complexes using integrative modeling platform. *Methods Mol. Biol.* **2022**, 353–377 (2019).
42. Kim, S. J. et al. Integrative structure and functional anatomy of a nuclear pore complex. *Nature* **555**, 475–482 (2018).
43. Jumper, J. et al. Highly accurate protein structure prediction with AlphaFold. *Nature* **596**, 583–589 (2021).
44. Varadi, M. et al. AlphaFold Protein Structure Database: massively expanding the structural coverage of protein-sequence space with high-accuracy models. *Nucleic Acids Res.* **50**, D439–D444 (2022).
45. Russel, D. et al. Putting the pieces together: integrative modeling platform software for structure determination of macromolecular assemblies. *PLoS Biol.* **10**, e1001244 (2012).

46. Tsai, S. C. et al. Crystal structure of the macrocycle-forming thioesterase domain of the erythromycin polyketide synthase: versatility from a unique substrate channel. *Proc. Natl Acad. Sci. USA* **98**, 14808–14813 (2001).
47. Gokulan, K., Aggarwal, A., Shipman, L., Besra, G. S. & Sacchettini, J. C. Mycobacterium tuberculosis acyl carrier protein synthase adopts two different pH-dependent structural conformations. *Acta Crystallogr. D* **67**, 657–669 (2011).
48. Keatinge-Clay, A. T. et al. Catalysis, specificity, and ACP docking site of *Streptomyces coelicolor* malonyl-CoA:ACP transacylase. *Structure* **11**, 147–154 (2003).
49. Tsai, S.-C., Lu, H., Cane, D. E., Khosla, C. & Stroud, R. M. Insights into channel architecture and substrate specificity from crystal structures of two macrocycle-forming thioesterases of modular polyketide synthases. *Biochemistry* **41**, 12598–12606 (2002).
50. Mindrebo, J. T. et al. Gating mechanism of elongating β-ketoacyl-ACP synthases. *Nat. Commun.* **11**, 1727 (2020).
51. Portevin, D. et al. The acyl-AMP ligase FadD32 and AccD4-containing acyl-CoA carboxylase are required for the synthesis of mycolic acids and essential for mycobacterial growth: identification of the carboxylation product and determination of the acyl-CoA carboxylase components. *J. Biol. Chem.* **280**, 8862–8874 (2005).
52. La Rosa, V. et al. MmpL3 is the cellular target of the antitubercular pyrrole derivative BM212. *Antimicrob. Agents Chemother.* **56**, 324–331 (2012).
53. Poce, G. et al. Improved BM212 MmpL3 inhibitor analogue shows efficacy in acute murine model of tuberculosis infection. *PLoS ONE* **8**, e56980 (2013).

Methods

Pks13 fusion generation and culturing

The Pks13-eGFP fusion strain was generated by chromosomally tagging the C terminus of *Pks13* gene with a TEV cleavage site followed by eGFP in the *Ms recBCD*-mutant strain as described previously[15]. The Pks13-eGFP protein was expressed under the native promoter in *Ms* when the culture was grown in 7H9 media supplemented with 1% (v/v) 50% glucose, 1% (v/v) 50% glycerol and 0.05% (v/v) Tween 80 at 37 °C to an optical density (OD_{600}) of roughly 2. Cell pellets were washed three times with 1× PBS, frozen and reduced to powder by cryo-milling[54].

Fluorescence size-exclusion chromatography

Here, 1 g of lysed cell powder (finely ground *M. smegmatis* frozen cell pellet resulting in cell lysis) was resuspended in 12 ml of solubilization buffer (50 mM Tris HCl pH 7.5, 150 mM NaCl) and a Roche cOmplete ULTRA EDTA-free protease inhibitor cocktail tablet, and 1 µl of benzonase (26.4 units $µl^{-1}$, EMD Millipore) was added to help de-clump the lysate, which was stirred at 4 °C for 1 h. To seek a mode of solubilization, nondenaturing detergents β-DDM, glyco-diosgenin, digitonin and *N*-decyl-β-D-maltopyranoside that are often used for structure determination, and denaturing detergents Fos-choline 12 (FC12) and Triton X100 that are denaturing but harsher in solubilizing from membranes were separately added to aliquoted lysate to final 1% (w/v) and solubilized at 4 °C for 2 h. Unsolubilized materials were pelleted at 100,000*g* for 20 min, and samples were filtered with 0.22 µm filter before injection onto the column. Signals were detected at both 280 nm and 488 nm. A Superose 6 Increase 5/150GL column (GE Healthcare) was run at 0.05 ml min^{-1} where 40 µl of each detergent-solubilized sample was loaded with the mobile phase (50 mM Tris HCl pH 7.5, 150 mM NaCl, Roche cOmplete ULTRA EDTA-free protease inhibitor cocktail, 0.15 mM β-DDM). β-DDM solubilization achieved the most optimal solubilization of Pks13, and thus was used for purification of the protein.

Protein purification for cryo-EM studies

Here, 10 g of cryo-milled lysed cell powder (finely ground *M. smegmatis* frozen cell pellet resulting in cell lysis) was resuspended in 100 ml buffer (50 mM Tris pH 7.5, 150 mM NaCl, 1% β-DDM, one tablet of Roche cOmplete ULTRA EDTA-free protease inhibitor cocktail). Next, 10 µl of benzonase (26.4 units $µl^{-1}$, EMD MilliporeSigma) was added and the solution was stirred at 4 °C for 2 h to solubilize membrane-tethered Pks13. The lysate containing Pks13 was spun at 100 kg for 30 min at 4 °C. Supernatant containing Pks13 was incubated with 5 ml of anti-GFP nanobody beads at 4 °C for 1.5 h to allow GFP-tagged Pks13 to bind to the anti-GFP nanobody beads. Anti-GFP nanobody beads were prepared by first expressing and purifying the anti-GFP nanobody protein from *Escherichia coli* BL21(DE3) and conjugating to NHS-Activated Sepharose 4 Fast Flow (Cytiva) following the manufacturer's protocol for conjugation. Pks13-GFP bound anti-GFP nanobody beads were washed three times with 30 ml of buffer (50 mM Tris pH 7.5, 150 mM NaCl, 0.2% β-DDM), with 3 min of shaking for each wash to remove nonspecifically bound protein(s). Washed anti-GFP nanobody beads were resuspended in 18 ml of buffer (50 mM Tris pH 7.5, 150 mM NaCl, 0.2% β-DDM) and incubated with roughly 1:10 TEV:Pks13 weight ratio of TEV enzyme overnight with gentle shaking at 4 °C to cleave off the C-terminal GFP tag from Pks13. Cleavage of Pks13 from GFP using TEV protease yielded full-length Pks13 with an additional five-amino acid linker (-SKSTS-) followed by six amino acids from the TEV cleavage site at its C terminus. TEV-cleaved Pks13 protein sample was concentrated and purified on a Superose 6 increase 10/300GL column (GE Healthcare) with buffer (50 mM Tris pH 7.5, 150 mM NaCl and Roche cOmplete ULTRA EDTA-free protease inhibitor cocktail), at a 0.3 ml min^{-1} flow rate (Extended Data Fig. 1a). Fractions containing the Pks13 first peak were pooled and concentrated to 1.5 mg ml^{-1} (4 µM). The TAM16 inhibitor of the terminal TE[17] was prepared as a 50 mM stock in dimethylsulfoxide and added to the 4 µM protein sample to a final 40 µM concentration with the aim of stabilizing and ordering the TE domains. Inhibitor and Pks13 protein were incubated together at 4 °C for 1 h before cryo-EM grid preparation.

Cryo-EM sample preparation

The Pks13 sample was concentrated to 1.5 mg ml^{-1} for cryo-EM grid preparation. Next 4.5 µl of the sample was applied to freshly glow discharged holey carbon on gold R1.2/1.3 300 mesh Quantifoil grids and blotted for 9 s with Whatman 1 filter paper at maximum humidity and 10 °C in a FEI Mark IV Vitrobot, before vitrification in liquid nitrogen-cooled liquid ethane.

Image acquisition

Grids were loaded onto an FEI Titan Krios G3 (at the University of California, San Franciso (UCSF)) operating at 300 kV, equipped with a K3 BioQuantum imaging system, using a 20 eV energy slit at UCSF. Imaging was performed in nanoprobe mode using a 70 µm C2 aperture, with a roughly 1.3 µm parallel illuminated area, without an objective aperture. The nominal energy filtered transmission electron microscope magnification was ×105,000, resulting in a super-resolution pixel size on the specimen of 0.4175 Å pix^{-1}. The dose rate was 8 e^{-} pix^{-1} s^{-1} with a total exposure time of 5.9 s, fractionated into 117 frames using correlated double sampling. Videos were acquired semiautomatedly with Serial-EM, using 3 × 3 hole beam-shift image-shift, over a nominal underfocus range of 0.7 to 1.5 µm. The super-resolution videos were drift corrected and dose weighted using UCSF MotionCor2 (ref. [55]) and twice Fourier binned to a pixel size of 0.835 Å pix^{-1}.

Image processing

A total of 7,567 dose weighted images were imported into cryoSPARC v.2.12 (ref. [56]) and contrast transfer function estimation was performed in patches. Then 4.4×10^6 particles were picked ab initio and extracted using a 386 pixel box and subjected to 2D classification from which 1.2×10^6 particles were retained. The particle set was then used to calculate an ab initio 3D volume that showed high-resolution features and quasi-C2 symmetry. The initial volume, low pass filtered to 30 Å was used as a reference for global angular refinement, without imposition of symmetry. Sequential refinement of beam tilt, defocus, Cs, trefoil and tetrafoil resulted in a nominal 2.0 Å reconstruction by GSFSC using a 0.143 criterion. Resolution-limited refinement in *cis*-transmission electron microscope[57] also produced a 2.0 Å reconstruction.

The same procedure was also repeated with imposition of C2 symmetry resulting in a nominal 1.9 Å reconstruction of the KS-AT didomain, and density modification in Phenix resolve_cryo_em[58,59] produced a map with 1.8 Å resolution, which we used for model building (Fig. 2a). These particle data were exported to RELION v.3.0 (ref. [60]) for symmetry expansion and focused classification. The C2 map was filtered and segmented in UCSF Chimera[61,62] for selection of domains to focus on. These maps were used to calculate cosine-edged masks using 'relion_mask_create'. The particle stack was C2 expanded using 'relion_particle_symmetry_expand', and classified against the C2 map, using masks for the ACPs, AT and KS-AT domains, without angular searches, varying the regularization parameter tau from 8 to 20. The particle subsets that provided the best visual features of each respective domain from each classification were selected and further refined using local angular searches and masking over the region of interest. This procedure produced the following maps at respective GSFSC resolutions: ACP1a-KS-AT map at 2.4 Å, ACP1b-KS-AT map at 2.6 Å, $KS\text{-}AT_{in}$ map at 3.0 Å and $KS\text{-}AT_{out}$ map at 3.1 Å (Fig. 2b). To assist with model building and interpretation, B factor modified maps were calculated using Phenix AutoSharpen[63] for the ACP1a-KS-AT and ACP1b-KS-AT maps. $KS\text{-}AT_{in}$ and $KS\text{-}AT_{out}$ maps were modified with DeepEMhancer[64].

Model building and refinement

Pks13 KS and AT core domains were built de novo using a Phyre2-generated homology model[65] as a guide. ACP1a and the DE-rich

linker were built into the density de novo guided by aromatic side chain densities for residues W9, W13, F62 and W90. ACP1b was similarly built into density.

Model building and refinement were performed using Coot[66], ISOLDE[67] and phenix_real_space_refine[68] using a combination of sharpened and density-modified volumes. KS-AT didomain was finally refined against the density-modified map from Phenix resolve-cryo-EM, and ACP1a-KS-AT, ACP1b-KS-AT were finally refined against *B* factor modified maps from Phenix AutoSharpen, and KS-AT_{in}, KS-AT_{out} were finally refined against sharpened maps from DeepEMhancer. All map and model figures were prepared using UCSF Chimera[61] and ChimeraX[62]. MOLE[69] was used to calculate the tunnels reported in the models.

Analysis of fatty acids in PKS13 by alkaline hydrolysis and LC–MS

Chains attached to PKS13 were determined by mass spectrometry. Negative ion ESI mass spectra of fatty acids released by hydrolysis are shown (Supplementary Figs. 6–8), along with their chemical structures and corresponding molecular formulas of the major species. Fatty acids are primarily detected as the deprotonated $[M-H]^-$ ions, along with lower levels of the chloride adduct $[M+Cl]^-$ ions. Hence the fatty acids are determined in the negative ion mode, being 1 Da less than the neutral species as listed in the figures.

To remove the fatty acids from the protein, the Pks13 protein sample was subjected to mild alkaline hydrolysis in 3.8 ml of chloroform/methanol:0.4 N KOH (1:2:0.8, v/v) at room temperature for 1 h. The system was converted to a two-phase Bligh/Dyer mixture consisting of chloroform/methanol/water (2:2:1.8, v/v/v) by adding appropriate volumes of chloroform and water. The lower phase was dried under a stream of nitrogen and stored at −20 °C before further analysis. Lipid analysis by normal phase LC–ESI/MS was performed as described[70] using an Agilent 1200 Quaternary LC system coupled to a high-resolution TripleTOF5600 mass spectrometer (Sciex). An Ascentis Si high-performance liquid chromatography column (5 µm, 25 cm × 2.1 mm, Sigma-Aldrich) was used. Mobile phase A consisted of chloroform:methanol:aqueous ammonium hydroxide (800:195:5, v/v/v). Mobile phase B consisted of chloroform:methanol:water:aqueous ammonium hydroxide (600:340:50:5, v/v/v/v.). The mobile phase C consisted of chloroform:methanol:water:aqueous ammonium hydroxide (450:450:95:5, v/v/v/v). The elution program was as follows: 100% mobile phase A was held isocratically for 2 min and then linearly increased to 100% mobile phase B for 14 min and held at 100% B for 11 min. The LC gradient was then changed to 100% mobile phase C for 3 min and held at 100% C for 3 min, and finally returned to 100% A over 0.5 min and held at 100% A for 5 min. Instrumental settings for negative ion ESI and MS/MS analysis of lipid species were as follows: ion spray voltage (IS) = −4,500 V; current gas (CUR) = 20 psi (pressure); gas-1 (GS1) = 20 psi; declustering potential (DP) = −55 V and focusing potential (FP) = −150 V. The MS/MS analysis used nitrogen as the collision gas. Data acquisition and analysis were performed using the Analyst TF1.5 software (Sciex).

Based on exact mass measurement, three fatty acid series were identified, (1) C51–C57 long (Supplementary Fig. 6), (2) C36–C42 in length (Supplementary Fig. 7) and (3) C22–C26 length (Supplementary Fig. 8). (1) The C51–C57 series are consistent with α2-meromycolate as the substrate for which the proximal portion is seen attached to the active site cysteine C267 of KS in the structure (Fig. 4). It could theoretically also have been consistent with being released from attachment to the ACP1 Ppant extension before *trans*-thioesterification and delivery to the KS. However, no modification is seen in the ACP1 structure arguing against this possibility. Therefore, we conclude that it is the species attached to the KS, hence the system has been captured before the Claisen condensation. This mass could have also been consistent with a cyclopropane in the aliphatic chain. However, cyclopropanes are not produced in *M. smegmatis* hence the assignment to the methyl substituent next to the double bond is assured. (2) A very long chain (C36–C42) with a *cis* double bond in the chain is consistent with the 'alpha-prime' mycolate found in *Ms* but not in *Mtb*[20]. This chain also is an alternative chain derived from the KS active center. (3) C22–26 fatty acids are fully saturated and most consistent with the α-branch species seen in density attached to the AT active center at serine S798. An additional possibility is that some of this species might also have been removed from the ACP2 before the Claisen condensation although the ACP2 is not defined in the Pks13 structure. The mass spectra of C22–C26 fatty acids do not contain the expected alpha-carboxyl group that is seen in the structure. The carboxyl may have been unstable at some part of the hydrolysis or during mass spectrometry.

Analysis of Pks13 complexes in solution DSSO cross-linking and multi-stage mass spectrometry (XL–MS^3)

We used a DSSO-based XL–MS^3 approach[35,36], wherein DSSO covalently cross-links primary amines of the side chains of lysines (K) or the N terminus of the protein. Following enzymatic digestion, the resulting peptides are separated by LC and analyzed by multi-stage MS: (1) intact peptide ions are measured at the MS1 stage; (2) using a lower energy collision-induced dissociation the DSSO backbone is cleaved while leaving peptide backbones intact, and the resulting fragment ions are measured at the MS2 stage and (3) each resulting ion is isolated in the instrument and the peptide backbone is fragmented using standard higher-energy C-trap dissociation (HCD) for peptide sequencing at the MS3 stage. Using this approach, we were able to distinguish between interlinked and 'dead-end' or monolinked peptides[71]. Interlinked peptides are the result of two cross-linked epsilon amino groups of lysine side chains (or the N-terminal alpha amino group) that cross-link two separate peptide species (α and β). Monolinked peptides are formed when a lysine or the N terminus reacts with DSSO, and before a second residue can form a bridge, the DSSO hydrolyzes resulting in a dead end.

Pks13 protein complexes were purified from *M. smegmatis* the same way as for cryo-EM sample preparation except for the TAM16 addition. Purified Pks13 complexes were cross-linked with increasing amounts of DSSO solubilized in anhydrous dimethylsulfoxide (Supplementary Table 3). The first replicate was prepared in duplicate, with both replicates cross-linked for 30 min at 1,000 r.p.m., one at 37 °C and one at 4 °C, with the following molar ratios of DSSO to complex: 1:10; 1:50; 1:250 and 1:1,000. Based on the similarity between DSSO cross-linking at 37 °C and one at 4 °C for Pks13, replicate 3 and 4 were cross-linked for 30 min at 1,000 r.p.m. at 37 °C only with the following molar ratios: 1:50; 1:250 and 1:1,000. Cross-linking reactions were quenched with 50 mM Tris pH 8, and then mixed with 4× SDS–PAGE loading buffer to a final 1× concentration (1× SDS–PAGE loading buffer: 62.5 mM Tris pH 6.8, 2% SDS, 75 mM DTT, 7.5% glycerol and 0.02% bromophenol blue). Protein samples were then separated by SDS–PAGE on 4–20% Criterion TGX gels (BioRad), stained by AcquaStain (Bulldog Bio) MS safe blue protein stain and bands excised for in gel digest (Supplementary Fig. 9). Gel pieces were cut to 1 mm^2 cubes, dehydrated, rehydrated in 15 mM TCEP, 25 mM NH_4HCO_3 reducing buffer and alkylated in 50 mM chloroacetamide in the dark. Gel pieces were dehydrated and rehydrated in 0.5 ng μl^{-1} trypsin buffer for protein digest. Peptides were extracted from the gel pieces with 50% acetonitrile (ACN), 5% formic acid, dried and resolubilized in 3% ACN, 2% formic acid. Resolubilized peptides were separated using an Easy-nLC 1200 (Thermo Fisher Scientific) on a 75 µm × 30 cm fused silica IntregraFrit capillary column (New Objective) packed in-house with 1.9-µm Reprosil-Pur C18 AQ reverse-phase resin (Dr. Maisch-GmbH), or a 15 cm-long column containing 1.7 µm BEH (ethylene bridged hybrid) beads (Waters). Peptides were eluted from Reprosil-Pur C18 AQ columns at 300 nl min^{-1} using the following linear gradient: 50–8% B in 5 min, 8–45% B in 35 min, 45–100% B in 12 min, 100% B for 5 min, 100–2% B in 2 min and 2% B for 2 min (mobile phase buffer A: 100% H_2O, 0.1% formic acid; mobile phase buffer B: 80% ACN, 0.1% FA). Peptides were eluted from BEH columns at 300 nl min^{-1} using the following linear

gradient: 5–22% B in 40 min, 22–32% B in 5 min, 32–100% B in 5 min and 100% B for 10 min (mobile phase buffer A: 100% H_2O, 0.1% formic acid; mobile phase buffer B: 80% ACN, 0.1% FA). Each sample was analyzed in technical duplicate by two independent MS^3 methods on an Orbitrap Fusion Lumos (Thermo Fisher Scientific) operated in positive ion mode. In one method, a single acquisition cycle consisted of nine scan events: (1) one full MS1 scan in the orbitrap (350–1,200 *m/z*, 60,000 resolution, maximum injection time of 50 ms); (2) two data-dependent MS2 scans in the orbitrap (30,000 resolution, normalized automatic gain control (AGC) target at 200%, isolation window 1.6 *m/z*) with normalized collision energy set at 22% on the top two precursor ions and (3) four MS3 scans in the ion trap (isolation window 2.5 *m/z*, standard AGC target, auto maximum injection time, rapid scan rate) with HCD collision energy set at 30% on the top four ions from each MS2 scan. In the second method, a single acquisition cycle was allowed 3 s and consisted of: (1) full MS1 scan in the orbitrap (350–1,200 *m/z*, 120,000 resolution, maximum injection time of 100 ms); (2) data-dependent MS2 scans in the orbitrap (30,000 resolution, normalized AGC target at 200%, isolation window 1.6 *m/z*) with normalized collision energy set at 22% on the top two precursor ions; and (3) four MS3 scans in the ion trap (isolation window 2.5 *m/z*, standard AGC target, auto maximum injection time, rapid scan rate) with HCD collision energy set at 30% on the top four ions from each MS2 scan. For both MS methods ions with charge state 4 to 8 were sampled for MS2 and dynamically excluded for 20 s (tolerance of 10 ppm), and ions with charge state 2 to 6 with precursor ions (5 *m/z* tolerance) excluded were selected for MS3.

Cross-linked peptides were analyzed as described in Kaake et al.[38]. In total, we identified 1,435 interlinks and 2,300 dead-end links including redundant counts, with a false positive rate of 1% as calculated by the identification of decoys (Supplementary Table 5 and Supplementary Fig. 10a). This included a small number of linkages between identified contaminating proteins (29 interlinks and 53 monolinks) (Supplementary Table 5). In total, the number of redundant Pks13 interlinks corresponded to 96 unique K-K linkages, 63 of which could be mapped to the ACP1a or ACP1b configurations of Pks13 with 50.8% of those found within the expected α carbon distance of 35 Å, and a high number of long-distance violations (>50 Å) (Supplementary Table 6 and Supplementary Fig. 10b). Among the 96 unique linkages we identified eight that could only come from oligomeric structures between at least two dimers of Pks13, all of which when mapped to either the ACP1a or the ACP1b configurations of Pks13 were beyond expected distances. Suspecting that some of the highly cross-linked samples were the product of aggregation or higher order oligomeric structures, we reanalyzed the data but removed the data files that were associated with highly cross-linked samples (Supplementary Table 2 and Supplementary Fig. 9). Using this filtered XL–MS^3 dataset, we identified 604 redundant interlinks that corresponded to 57 unique linkages (Supplementary Table 2 and Supplementary Fig. 10c). This corresponded to 33 linkages that mapped to ACP1a or ACP1b configurations, with 67% of those within the expected distances, and only one long-distance violation (Supplementary Table 2 and Supplementary Fig. 10d). Most of the violations can be accounted for by small movements or flexibility in the structure. To model the domains not seen in ACP1a or ACP1b configurations, and to capture flexibility in the in-solution structure, we used the 57 unique linkages (Extended Data Fig. 9) from the filtered XL–MS dataset for integrative modeling.

The proteomics data from each step of the analysis pipeline, including raw files, MS2 and MS3 extracted peak files (from MSConvert (ProteoWizard[72,73])), MS3 search files (from ProteinProspector v.6.2.17) and associated search and filtering parameters files, have been deposited to the ProteomeXchange Consortium via the PRIDE[74] partner repository with the dataset identifier PXD033471. Annotated spectra for all interlinked, dead-end and single peptides can be found on the MSViewer[75] application through ProteinProspector (https://msviewer.ucsf.edu/prospector/cgi-bin/msform.cgi?form=msviewer).

Integrative structure modeling of the Pks13 dimer

A structural model of the Pks13 in solution was computed by integrative modeling[39,42,76], based on atomic models of component domains obtained by cryo-EM and AlphaFold2 (refs. [43,44]) prediction as well as 57 unique DSSO cross-links. Integrative modeling proceeded through the standard four stages[38–41,77]: (1) gathering data; (2) representing subunits and translating data into spatial restraints; (3) structural sampling to produce an ensemble of models that satisfies the restraints; and (4) analyzing and validating the ensemble models as well as input information. The modeling protocol was scripted using the Python Modeling Interface package, a library for modeling macromolecular complexes based on our open-source Integrative Modeling Platform package[45] (https://integrativemodeling.org). Files containing the input data, scripts and output results are freely available at https://github.com/integrativemodeling/Pks13. The details about the approach are given in Supplementary Table 4.

Reporting summary

Further information on research design is available in the Nature Portfolio Reporting Summary linked to this article.

Data availability

The atomic coordinates for five structures of Pks13 have been deposited in the PDB with the accession codes 7UK4, 8CUY, 8CV1, 8CUZ and 8CV0. The corresponding maps have been deposited in the Electron Microscopy Data Bank with the accession codes EMD-26574, EMD-27002, EMD-27005, EMD-27003 and EMD-27004. Proteomics data have been deposited to the ProteomeXchange Consortium with the dataset identifier PXD033471. Files containing the input data, scripts and output results for integrative modeling are freely available at https://github.com/integrativemodeling/Pks13. The details about the approach are given in Supplementary Table 4. Source data are provided with this paper.

References

54. LaCava, J., Jiang, H. & Rout, M. P. Protein complex affinity capture from cryomilled mammalian cells. *J. Vis. Exp.* https://doi.org/10.3791/54518 (2016).
55. Zheng, S. Q. et al. MotionCor2: anisotropic correction of beam-induced motion for improved cryo-electron microscopy. *Nat. Methods* **14**, 331–332 (2017).
56. Punjani, A., Rubinstein, J. L., Fleet, D. J. & Brubaker, M. A. cryoSPARC: algorithms for rapid unsupervised cryo-EM structure determination. *Nat. Methods* **14**, 290–296 (2017).
57. Grant, T., Rohou, A. & Grigorieff, N. cisTEM, user-friendly software for single-particle image processing. *eLife* **7**, e35383 (2018).
58. Terwilliger, T. C., Ludtke, S. J., Read, R. J., Adams, P. D. & Afonine, P. V. Improvement of cryo-EM maps by density modification. *Nat. Methods* **17**, 923–927 (2020).
59. Afonine, P. V. et al. Real-space refinement in PHENIX for cryo-EM and crystallography. *Acta Crystallogr. D* **74**, 531–544 (2018).
60. Zivanov, J. et al. New tools for automated high-resolution cryo-EM structure determination in RELION-3. *eLife* **7**, e42166 (2018).
61. Pettersen, E. F. et al. UCSF Chimera—a visualization system for exploratory research and analysis. *J. Comput. Chem.* **25**, 1605–1612 (2004).
62. Goddard, T. D. et al. UCSF ChimeraX: meeting modern challenges in visualization and analysis. *Protein Sci.* **27**, 14–25 (2018).
63. Terwilliger, T. C., Sobolev, O. V., Afonine, P. V. & Adams, P. D. Automated map sharpening by maximization of detail and connectivity. *Acta Crystallogr. D* **74**, 545–559 (2018).
64. Sanchez-Garcia, R. et al. DeepEMhancer: a deep learning solution for cryo-EM volume post-processing. *Commun. Biol.* **4**, 874 (2021).

65. Kelley, L. A., Mezulis, S., Yates, C. M., Wass, M. N. & Sternberg, M. J. E. The Phyre2 web portal for protein modeling, prediction and analysis. *Nat. Protoc.* **10**, 845–858 (2015).
66. Emsley, P., Lohkamp, B., Scott, W. G. & Cowtan, K. Features and development of Coot. *Acta Crystallogr. D* **66**, 486–501 (2010).
67. Croll, T. I. ISOLDE: a physically realistic environment for model building into low-resolution electron-density maps. *Acta Crystallogr. D* **74**, 519–530 (2018).
68. van Zundert, G. C. P., Moriarty, N. W., Sobolev, O. V., Adams, P. D., & Borrelli, K. W. Macromolecular refinement of X-ray and cryoelectron microscopy structures with Phenix/OPLS3e for improved structure and ligand quality. *Structure* **29**, 913–921.e4 (2021).
69. Pravda, L. et al. MOLEonline: a web-based tool for analyzing channels, tunnels and pores (2018 update). *Nucleic Acids Res.* **46**, W368–W373 (2018).
70. Tan, B. K. et al. Discovery of a cardiolipin synthase utilizing phosphatidylethanolamine and phosphatidylglycerol as substrates. *Proc. Natl Acad. Sci. USA* **109**, 16504–16509 (2012).
71. Kao, A. et al. Development of a novel cross-linking strategy for fast and accurate identification of cross-linked peptides of protein complexes. *Mol. Cell Proteom.* **10**, M110.002212 (2011).
72. Chambers, M. C. et al. A cross-platform toolkit for mass spectrometry and proteomics. *Nat. Biotechnol.* **30**, 918–920 (2012).
73. Kessner, D., Chambers, M., Burke, R., Agus, D. & Mallick, P. ProteoWizard: open source software for rapid proteomics tools development. *Bioinformatics* **24**, 2534–2536 (2008).
74. Perez-Riverol, Y. et al. The PRIDE database and related tools and resources in 2019: improving support for quantification data. *Nucleic Acids Res.* **47**, D442–D450 (2019).
75. Baker, P. R. & Chalkley, R. J. MS-viewer: a web-based spectral viewer for proteomics results. *Mol. Cell Proteom.* **13**, 1392–1396 (2014).
76. Alber, F. et al. Determining the architectures of macromolecular assemblies. *Nature* **450**, 683–694 (2007).
77. Viswanath, S., Chemmama, I. E., Cimermancic, P. & Sali, A. Assessing exhaustiveness of stochastic sampling for integrative modeling of macromolecular structures. *Biophys. J.* **113**, 2344–2353 (2017).

Acknowledgements

We thank J. Sacchettini, Texas A&M University for the inhibitor TAM16 and C. Sassetti, University of Massachusetts Worcester for the Pks13-TEV-eGFP MSMEG strain and both for their insights, A. Keatinge-Clay and J. Sacchettini for their reading of the paper, counsel and advice, and G. Ashley, ProLynx, Inc. for Supplementary Fig. 1b. We acknowledge P. Thomas, M. Harrington, J. Baker-LePain and the Wynton HPC for computational support; and D. Bulkley, Z. Yu and G. Gilbert for their maintenance of the UCSF EM Core. We thank J. Wilkins and K. Li for performing initial mass spectrometry for lipid identification in the UCSF mass spectrometry core. Research was financially supported by grant nos. P01 AI095208 (J. Sacchettini), GM024485 (R.M.S.), AI48366 (Z.G.), GM083960 and GM109824 (A.S.), U19 A1135990 (N.J.K.) and R01 AI128214 (O.S.R.). M.S.D. acknowledges a National Science Federation graduate fellowship.

Author contributions

O.S.R., S.K.K. and R.M.S. conceived the project. S.K.K. and J.C. prepared the protein. M.S.D. prepared EM grids and performed EM imaging and image processing. M.S.D. interpreted density maps and determined the five structures reported. S.K.K., M.S.D. and J.F.-M. refined and interpreted the structures. Z.G. determined the lipid chains attached to PKS13 by mass spectrometry at 'the lipidomics project'. E.H.P., R.M.K. and N.J.K. determined the DSSO cross-links formed by mass spectrometry. I.E. and A.S. performed integrative structure determination. R.M.S. and O.S.R. supervised the project. S.K.K., M.S.D., J.F.M., Z.G., O.S.R. and R.M.S. wrote the paper with contributions from all authors.

Competing interests

The Krogan Laboratory has received research support from Vir Biotechnology, F. Hoffmann-La Roche and Rezo Therapeutics. N.J.K. has financially compensated consulting agreements with the Icahn School of Medicine at Mount Sinai, New York, Maze Therapeutics, Interline Therapeutics, Rezo Therapeutics, GEn1E Lifesciences, Inc. and Twist Bioscience Corp. He is on the Board of Directors of Rezo Therapeutics and is a shareholder in Tenaya Therapeutics, Maze Therapeutics, Rezo Therapeutics and Interline Therapeutics.

Additional information

Extended data is available for this paper at https://doi.org/10.1038/s41594-022-00918-0.

Supplementary information The online version contains supplementary material available at https://doi.org/10.1038/s41594-022-00918-0.

Correspondence and requests for materials should be addressed to Oren S. Rosenberg or Robert M. Stroud.

Peer review information *Nature Structural & Molecular Biology* thanks the anonymous reviewers for their contribution to the peer review of this work. Primary Handling Editor: Florian Ullrich and Carolina Perdigoto, in collaboration with the *Nature Structural & Molecular Biology* team.

https://doi.org/10.1038/s41594-022-00918-0

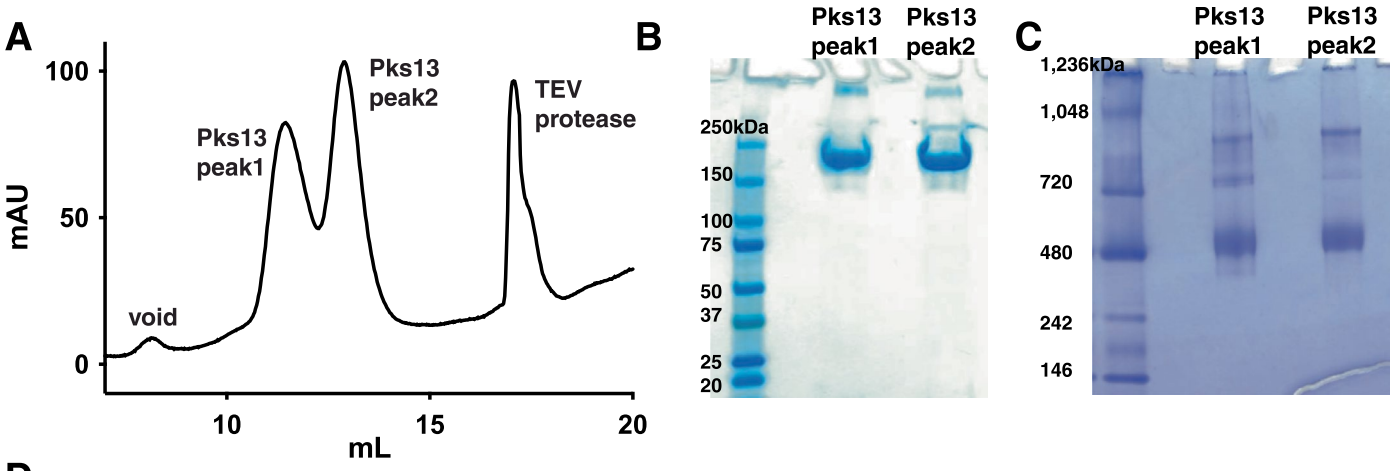

D

```
1    MTVNEMREWL RNWVANATGQ SADAIDESTP MVELGLSSRD AVAMASDIED LTGVTLTATV AFRHPTIESL ATVIIEGEPE
81   PEPYDEDEDW SRTRDVEDIA IVGVATRFPG DLNTPDEMWE ALLEGKDCVT DLPEDRWTEF LDEPRIAERV KKARTRGGYL
161  TDIKGFDSEF FALSKMEADN IDPQQRMALE LTWEALEHAR IPASSLRGES VGVYIGSSTN DYSFLAMSDP SIAHPYAITG
241  TASSIIANRV SYFYDFRGPS VAVDTACSSS LVATHQGVQA LRAGEADVAI VGGVNALVTP LVTVGFDEVG GVLAPDGRIK
321  SFSSDADGYA RSEGGGMLVL KRISDARRDG DQILAVIAGS AVNHDGRSNG LLAPNPDAQA EVLRKAYKDA GINPRDVDYI
401  EAHGTGTILG DPIEADALGR IVGKGRPADK PALLGAVKSN LGHLESAAGA ASLAKMTLAL ANDKLPPSIN YAGPNPYIDF
481  EKERLKVNDT VSDWPRYSGK AIAGVSGFGF GGANAHVVMR EVLAGDLVEP EPEPEPEAKP EKSEADAVYV GGVRMDEYGE
561  FIDEDEPAEG GDAYPSYDED SYELPGITEA AQRLLEQARE ELEAKEAEEP TKQLVPLAVS AFLTSRKRQA AAELADWIDS
641  PEGRASSLES IGRSLSRRNH GRSRAVVLAH DHDEAIKGLR ALAEGKQHPS VLSADGPVTN GPVWVLAGFG AQHRKMGKSL
721  YLRNEVFAEW INKVDALIQD ERGYSILELI LDDNVDYTDA TCEYPIEVVQ LVIFAIQIAL GELLRHHGAK PAAVVGQSLG
801  EAAASYFAGG LSLADATRTI CSRSHLMGEG EAMLFGEYIR LMALVEYSAD EIKTVFSDYP DLEVCVYAAP TQTVIGGPPD
881  QVDAIIARAE SEGKFARKFQ TKGASHTQQM DPLLGELAAE LQGIEPKPLT TGYFSTVHEG TFIRPGSAPI HDVDYWKKGL
961  RHSVYFTQGI RNAVDNGHTT FLELAPNPVA LMQVGLTTAS AGLHDAQLIA TLARKQDEVE SMISAMAQLY VHGHDLDFRT
1041 LFPRRSKGLA GALDFANIPP TRFKRKEHWL PAHFTGDSSA VMPGNHVATP DGRHVWEFVP RGKTDLAALV KAAAAQVLPD
1121 AKLAAFEQRA VPADNARLVT TLTRHPGGAT VQVHARVEES FTLVYDAIVA RANGAGVTAL PVAVGAGVAV SGDVAGEGAG
1201 ASVIEDDEPD AEILQDNLTA GAGMGADFQK WDPNSGETIG QRLGTIVGAA MGYEPEDLPW EVPLIELGLD SLMAVRIKNR
1281 VEYDFDLPPI QLTAVRDANL YNVEELIRYA IEHRDEVEQI AESQKGKTAE EIAAEQSELL GGASTVAELE AKLAEAGHPL
1361 AAKDSEDSEN SEDNAAGAAA AAEASAVEGL EIPPPPTDPT GPGGAPIPPP PSDPSGPAQA ASATDAPAGT VNKATAAAAA
1441 AKVLTQEAVT EALGADVPPR DAAERVTFAT WAIVTGKSPG GIFNELPTVS EETAKKMAER LSERAEGTIT VEDVLGAKTI
1521 EGLATIVREQ LEEGVVDGFV RTLRPPKEGS NAVPLFVFHP AGGSTVVYEP LMKRLPADVP VYGLERVEGS IEERAAEYVP
1601 KLLEMHKGPF VLAGWSLGGA LAYACAIGLK QSGADVRFVG LIDTVLPGEP IDQSKEGMRA RWDRYARFAE RTFNVEIPAI
1681 PYEELEKLDD EGQVKYVLEI VKESGVQIPG GIIEHQRTSY LDNRALDTVD IKPYDGHVTL YMADRYHDDA IVFEPAYATR
1761 KPDGGWGSFV SDLEVVHIGG EHIQAIDEPY IAKVGAHMSE ALNRIEAQAS KEDGAK
```

Num Unique	% Cov	Best Disc Score	Best Expect Val
242	78.1	14.32	6.6e-26

Extended Data Fig. 1 | Purification of native Pks13 from mycobacteria. (**a**) Final Superose 6 size exclusion chromatography profile of Pks13. Two peaks containing Pks13 are labeled 1 and 2, in addition to the void peak and peak containing TEV protease. Pks13 peaks were run on non-reducing SDS-PAGE (Biorad #4561096) (**b**) and blue native PAGE (Invitrogen #BN1004BOX) (**c**), which were repeated twice with similar results. In SDS-PAGE (**b**) the protein runs at ~198 kDa, as expected for a protomer of Pks13. Blue native PAGE (**c**) indicates that majority of the protein is in a dimeric form, and higher oligomeric forms are present. Upon screening both peaks 1 and 2 on gold Quantifoil grids by cryoEM, peak 1 was selected for data collection since it produced more monodisperse particles that correspond to Pks13 dimers. We conclude that the Pks13 dimers associate loosely in solution, and that these readily dissociate to form monodisperse Pks13 dimers under the conditions in which the images were acquired. (**d**) 78.1% sequence coverage (highlighted red) by tryptic digested Pks13 fragments run on LC-MS-MS.

https://doi.org/10.1038/s41594-022-00918-0

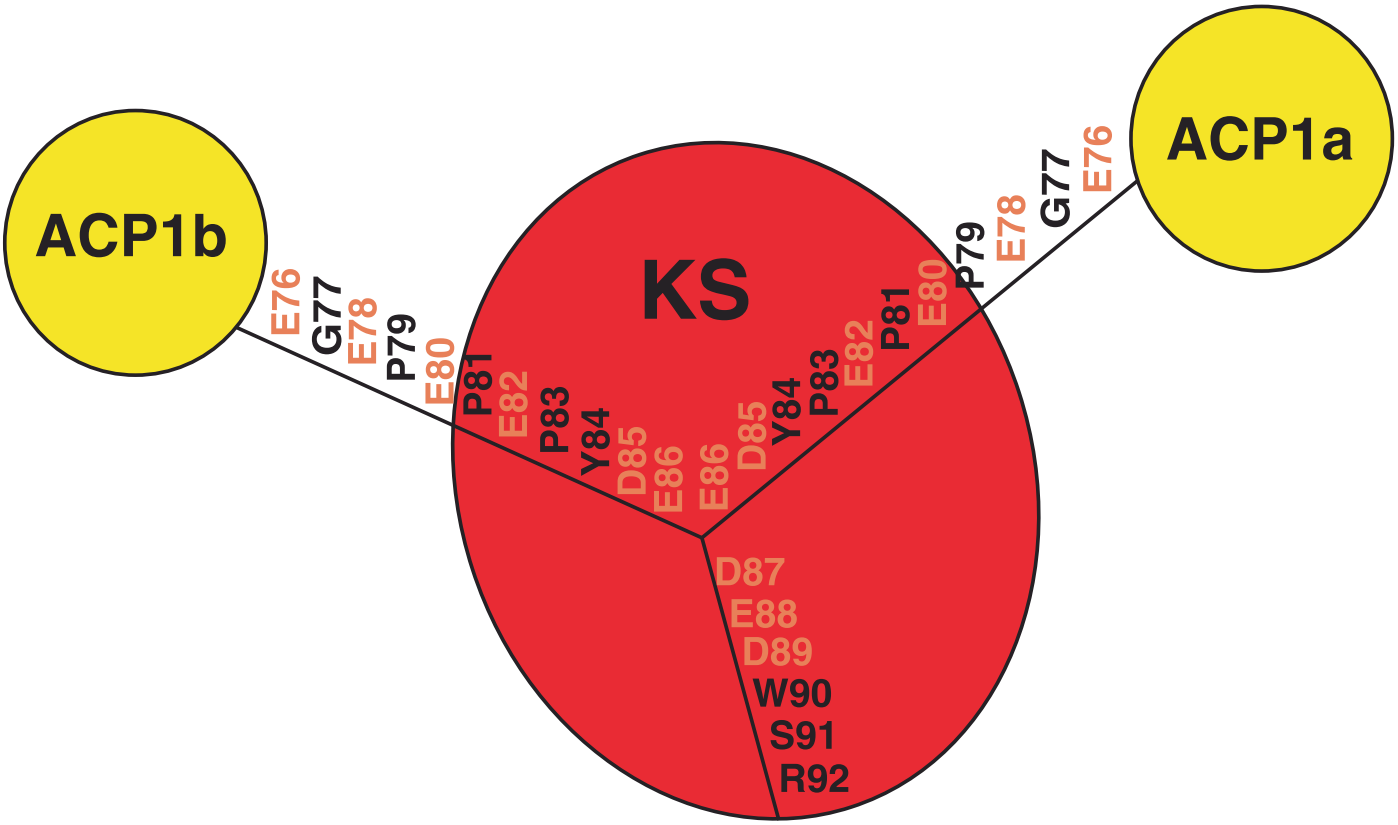

Extended Data Fig. 2 | DE-rich linker. 17 amino acid linking sequence (E76-92) between ACP1 and KS includes nine acidic amino acids (colored orange) and termed the 'DE-rich linker'. First 11 amino acids (E76-E86) lie near positively charged surfaces of two different regions on the KS monomer surface (Extended Data Fig. 3). The last six amino acids (D87-R92) closely overlap in orientation between the ACP1a and ACP1b structures and interact electrostatically with the shared positively charged surface (Extended Data Fig. 3).

https://doi.org/10.1038/s41594-022-00918-0

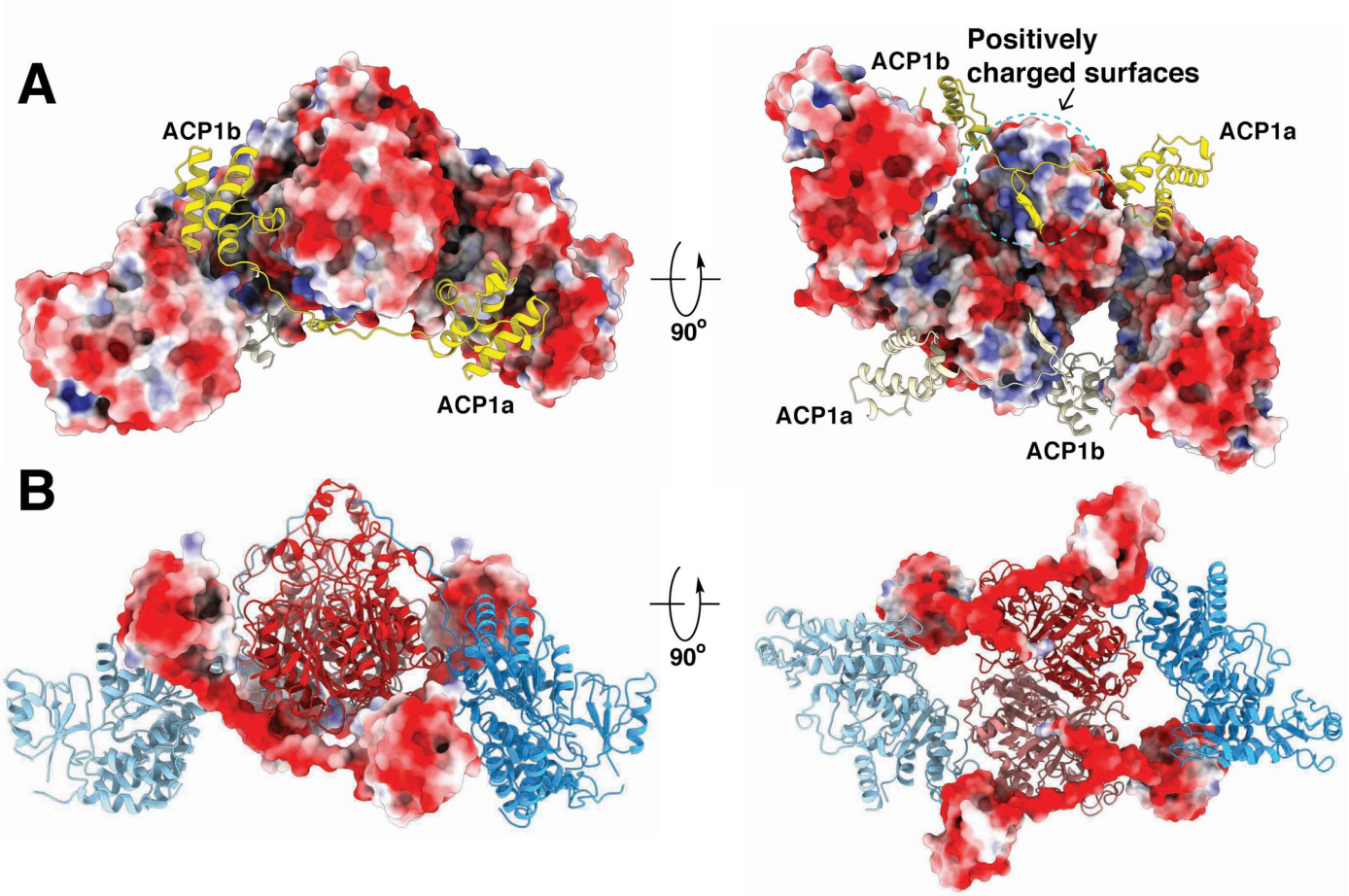

Extended Data Fig. 3 | Electrostatic surface rendering of ACP1-KS-AT domains. (**a**) The KS-AT surface is colored by electrostatic potential (red: acidic, blue: basic) of the residues. ACP1a and ACP1b and their ensuing linkers to the KS (yellow and lemon chiffon) are superimposed onto the KS-AT electrostatic potential surface, illustrating that the DE-rich linker lie near positively charged surfaces on the KS. (**b**) ACP1a, ACP1b, and the linkers to the KS are colored by electrostatic potential (red: acidic, blue: basic) of the residues. Model of KS-AT is superimposed onto the highly negative electrostatic potential surface of the DE-rich linker.

https://doi.org/10.1038/s41594-022-00918-0

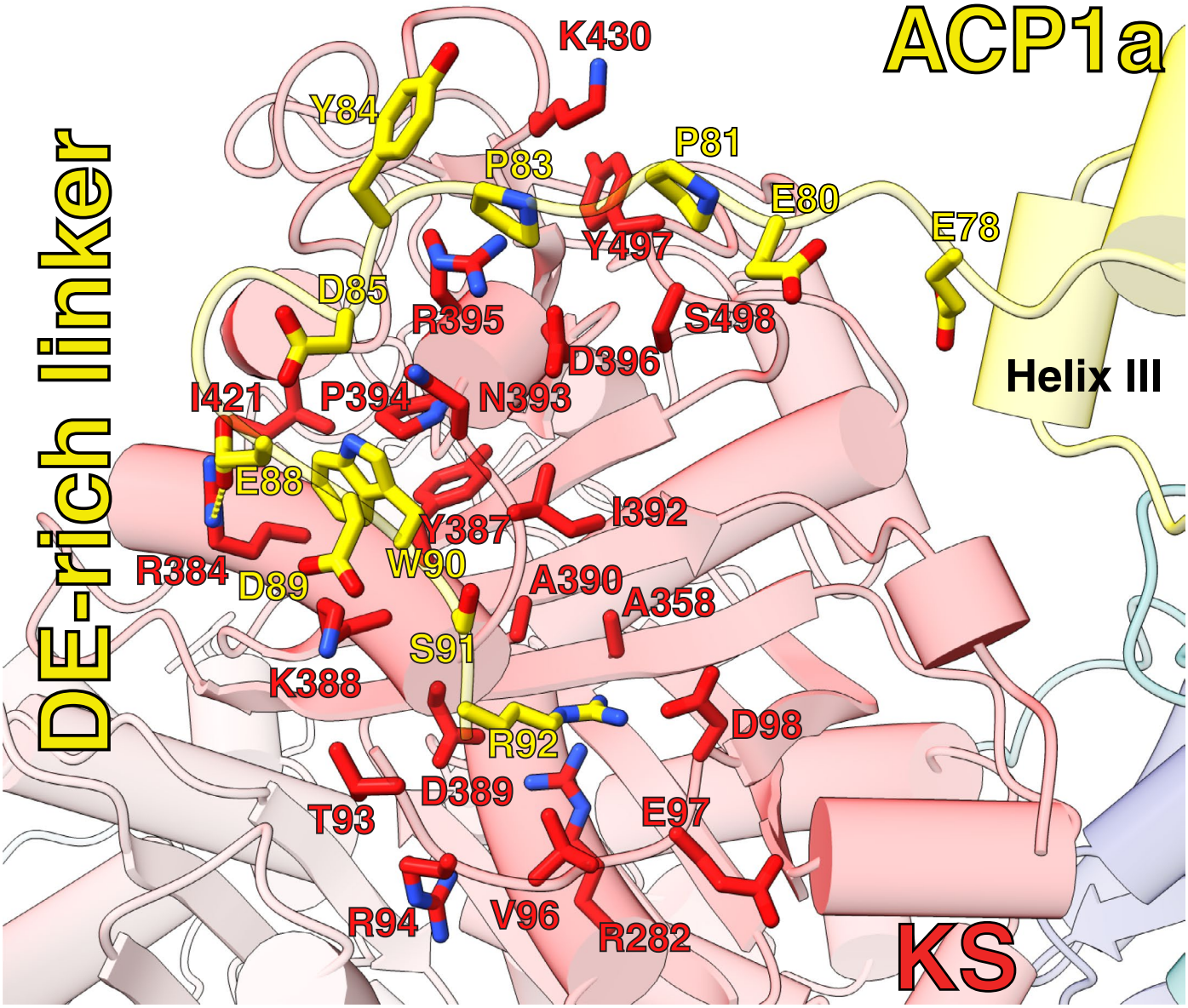

Extended Data Fig. 4 | Interfacing residues between DE-rich linker and KS domain in ACP1a position. Interfacing residues were determined by PISA and labeled. Hydrogen bond between E88(OE2):R384(NH2) is represented with a yellow dotted line.

https://doi.org/10.1038/s41594-022-00918-0

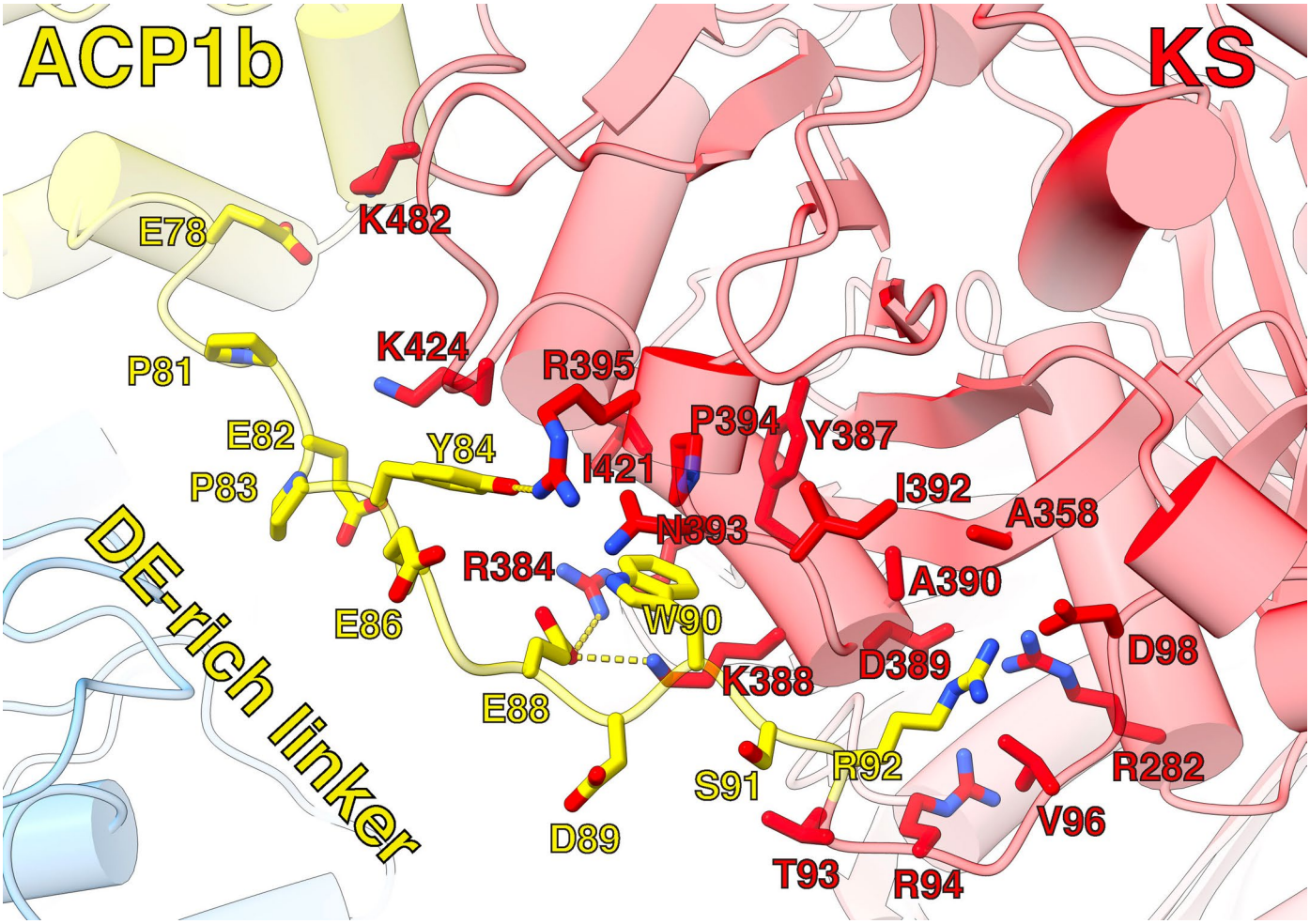

Extended Data Fig. 5 | Interfacing residues between DE-rich linker and KS domain in ACP1b position. Interfacing residues were determined by PISA and labeled. Hydrogen bonds between Y84(OH):R395(NH1), E88(OE2):R384(NH1), and E88(OE2):K388(NZ) are labeled with yellow dotted lines.

https://doi.org/10.1038/s41594-022-00918-0

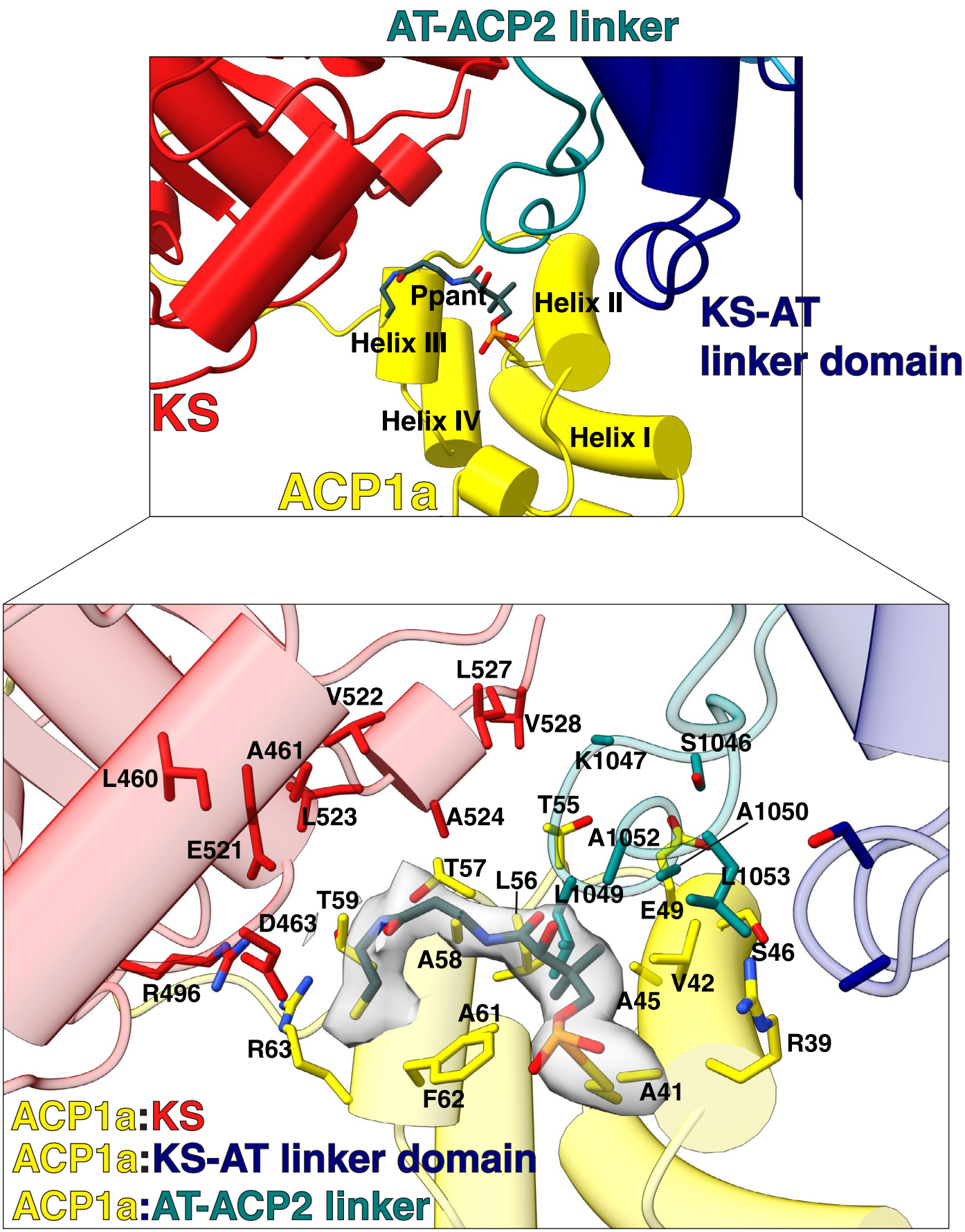

Extended Data Fig. 6 | See next page for caption.

https://doi.org/10.1038/s41594-022-00918-0

Extended Data Fig. 6 | ACP1a interaction with KS, KS-AT linker domain, and AT-ACP2 linker. Interfacing residues between ACP1a and KS, KS-AT linker domain, and AT-ACP2 linker are shown as stick representation and labeled. Pi-pi stacking interaction is shown between R63 of ACP1a and R496 of KS. The Ppant arm is shown attached to S38 in helix II of ACP1a, and Ppant density is shown zoned around 2.3 Å around the model.

https://doi.org/10.1038/s41594-022-00918-0

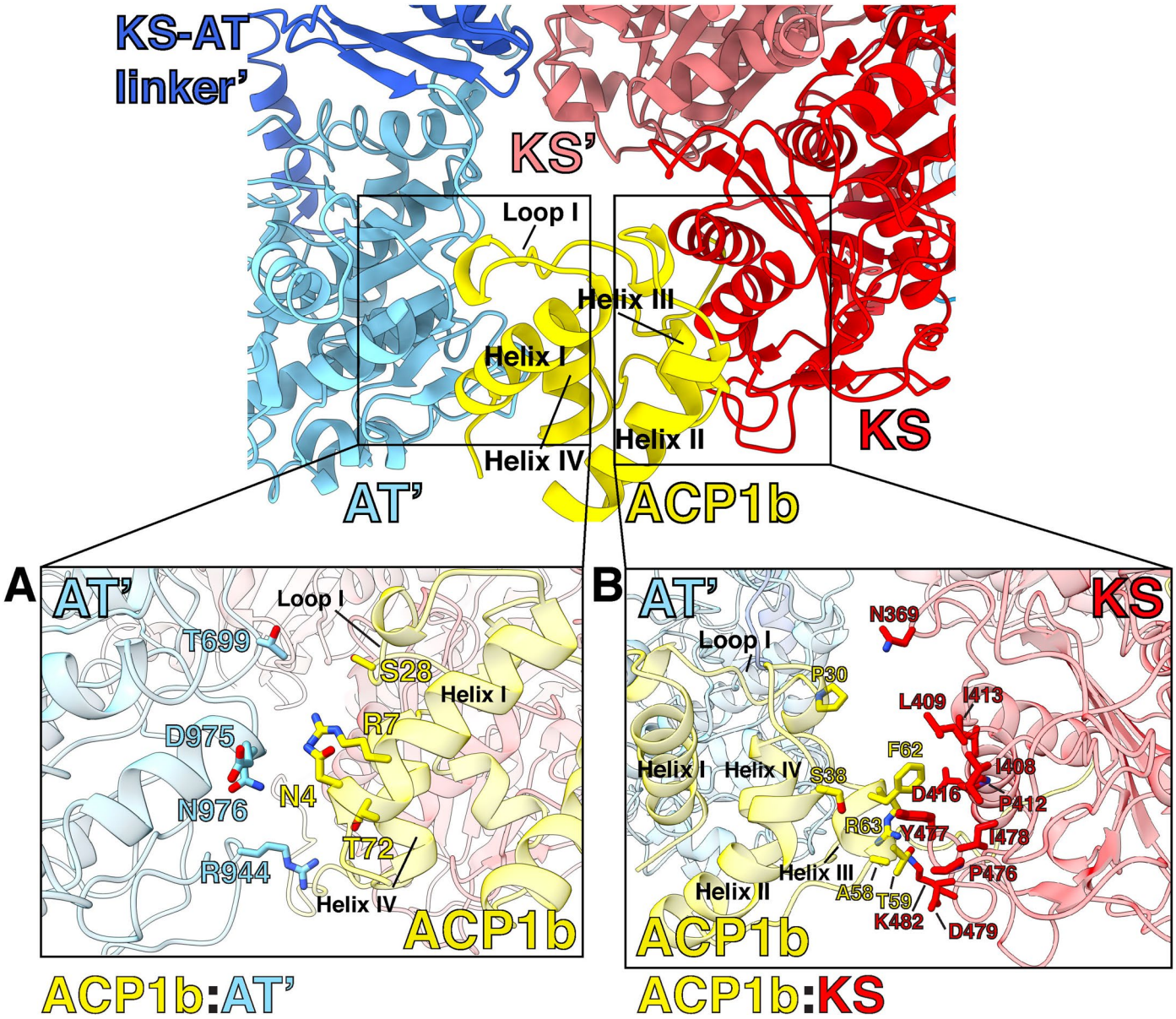

Extended Data Fig. 7 | ACP1b interaction with KS and AT'. (**a**) ACP1b:AT' interfacing residues' side chains are shown and labeled, revealing a hydrophilic interface. (**b**) ACP1b:KS interfacing residues' side chains are shown and labeled, revealing a hydrophobic interface.

https://doi.org/10.1038/s41594-022-00918-0

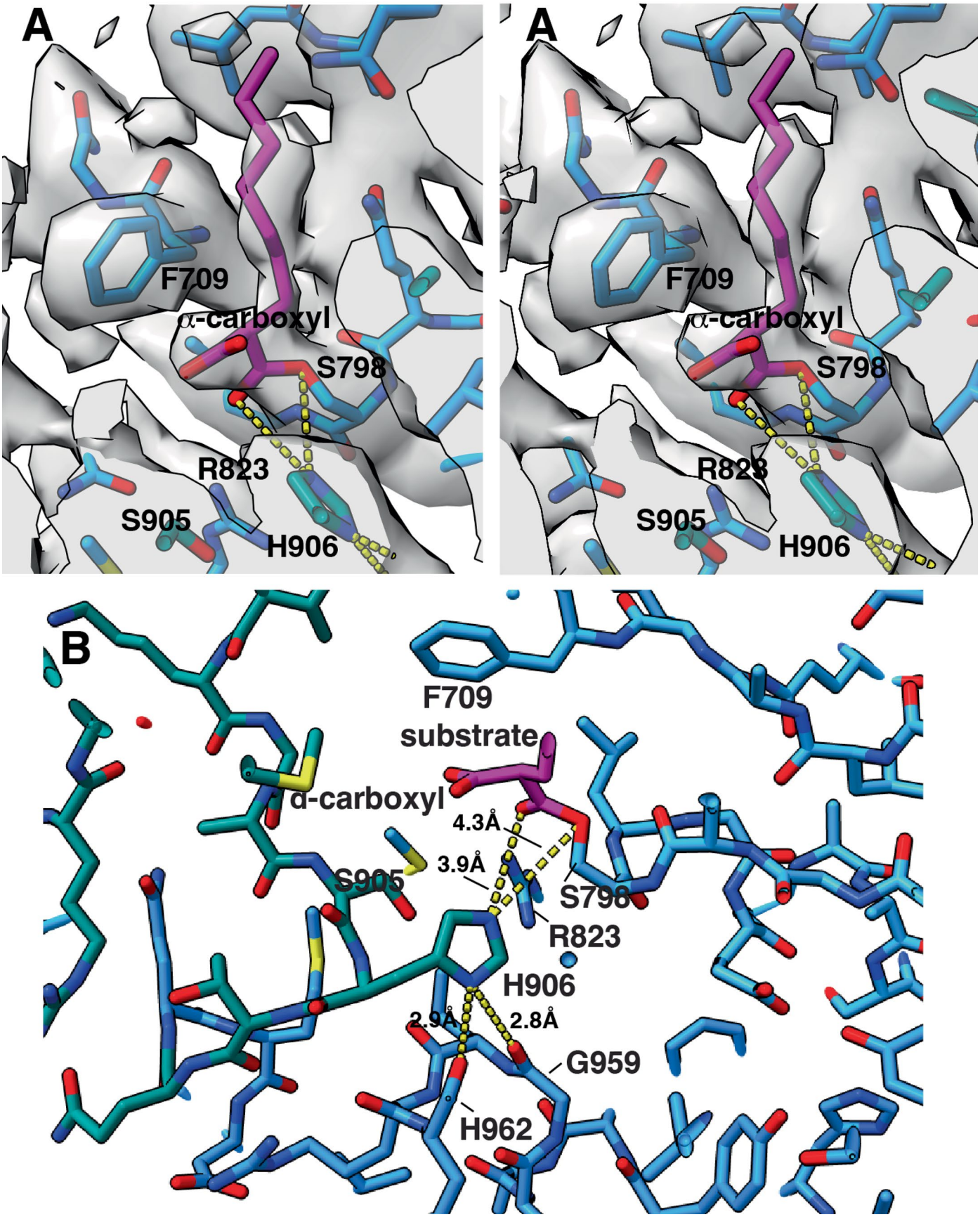

Extended Data Fig. 8 | See next page for caption.

https://doi.org/10.1038/s41594-022-00918-0

Extended Data Fig. 8 | The active center of the AT domain shows the bound substrate interactions. (**a**) Crossed-eyes stereo figure showing the density for the active site of the AT domain with substrate bound. The α-carboxyl group on the bound substrate is stabilized by a π-anion interaction with the phenyl ring of F709. (**b**) Rotated ~90° around the vertical axis and tilted forward from panel (**a**) shows interactions between the active center of the AT domain and the bound α-carboxy acyl substrate chain attached to S798. Distances between heavy atoms are tabulated in Å. The catalytic base H906 is ideally placed for the reaction at the γO of S798. The ester carbonyl on the substrate, and hence the oxyanion intermediate formed at that oxygen during the catalytic reaction may be stabilized by R823, H906, and S905. The H906 orientation is aligned by hydrogen bonds from the δN-H to the C = O of G959 and of H962.

https://doi.org/10.1038/s41594-022-00918-0

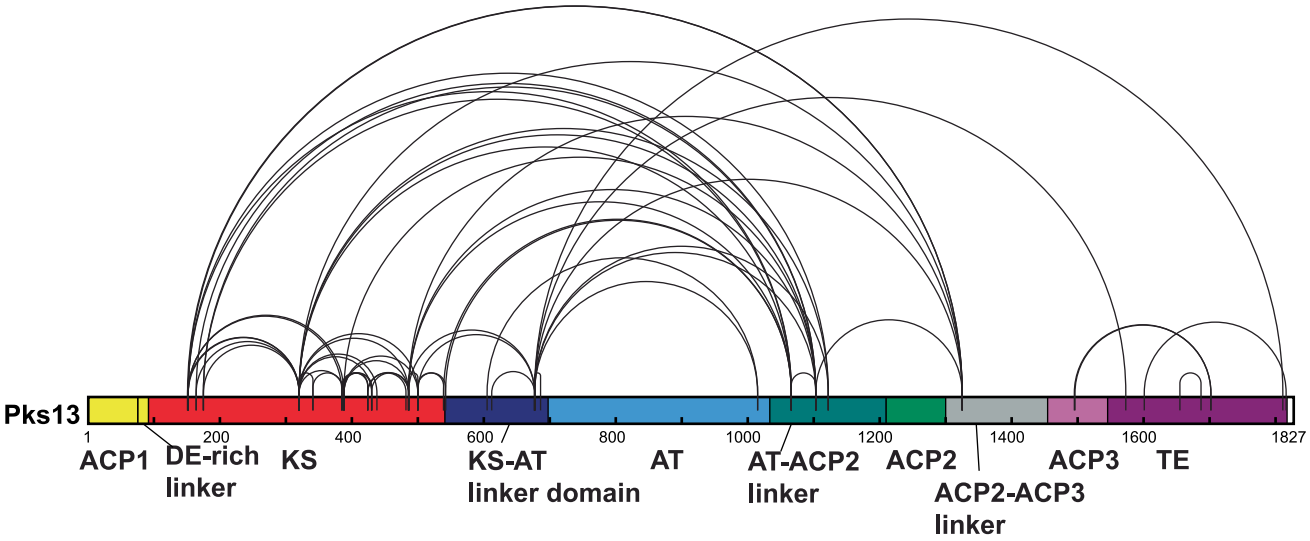

Extended Data Fig. 9 | Linkage map depicting all unique K-K linkages of DSSO cross-linked Pks13. The 57 unique K-K inter-linked residues are summarized in this linkage map as black lines connecting two Pks13 lysine residues. Shown is a cartoon diagram of the primary sequence structure of Pks13 with domains labeled as in Fig. 1a. The sequence numbers of lysine residues indicated by linear position in this figure are included in Supplementary Tables 2, 3, 5, and 6.

https://doi.org/10.1038/s41594-022-00918-0

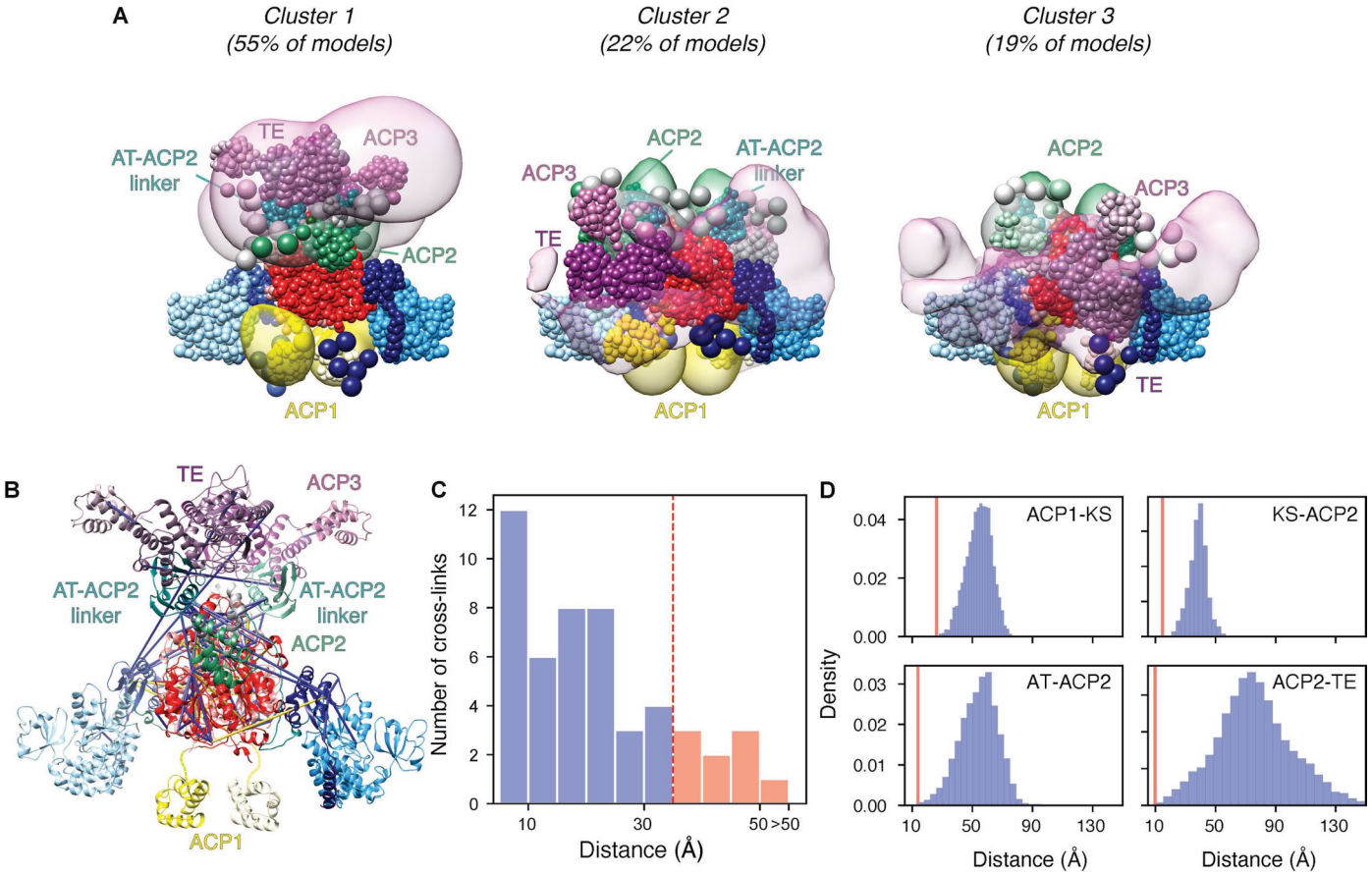

Extended Data Fig. 10 | Integrative structure modeling of the full-length Pks13 dimer. (**a**) The localization probability density of the ensemble of structures is shown with representative (centroid) structure from the ensemble embedded within it. The three panels represent different solutions with their relative percentages listed above. The structured and unstructured regions are represented as beads, using the same color scheme as Fig. 1a. Regions with well-defined structures are modeled as rigid bodies consisting of beads representing each individual residue; the coordinates of a 1-residue bead were those of the corresponding Cα atom. Regions with no available structure or flexible regions are represented as flexible strings of beads, corresponding to up to 10 residues per bead. (**b**) Detail of cross-links mapped to the centroid structure of the integrative model of the Pks13 dimer. Satisfied and violated cross-links shown in blue and yellow, respectively. A cross-link is classified as satisfied if the Cα–Cα distance spanned by the cross-linked residues in any of the models of the cluster is less than 35 Å. (**c**) Histogram showing the distribution of the cross-linked Cα–Cα distances in the Pks13 dimer integrative structures. (**d**) Histogram showing the Cα–Cα distances between the active sites of the ACP1-KS, AT-ACP2, KS-ACP2, and ACP2-TE domains. The shortest distances (red lines) are 26, 13.7, 14.8, and 9.7 Å between the ACP1-KS, AT-ACP2, KS-ACP2, and ACP2-TE domains, respectively.

nature portfolio

Corresponding author(s): DBPR NSMB-A45979A STROUD ROSENBERG

Last updated by author(s): Oct 18, 2022

Reporting Summary

Nature Portfolio wishes to improve the reproducibility of the work that we publish. This form provides structure for consistency and transparency in reporting. For further information on Nature Portfolio policies, see our Editorial Policies and the Editorial Policy Checklist.

Statistics

For all statistical analyses, confirm that the following items are present in the figure legend, table legend, main text, or Methods section.

n/a	Confirmed	
☒	☐	The exact sample size (*n*) for each experimental group/condition, given as a discrete number and unit of measurement
☒	☐	A statement on whether measurements were taken from distinct samples or whether the same sample was measured repeatedly
☐	☒	The statistical test(s) used AND whether they are one- or two-sided *Only common tests should be described solely by name; describe more complex techniques in the Methods section.*
☒	☐	A description of all covariates tested
☐	☒	A description of any assumptions or corrections, such as tests of normality and adjustment for multiple comparisons
☒	☐	A full description of the statistical parameters including central tendency (e.g. means) or other basic estimates (e.g. regression coefficient) AND variation (e.g. standard deviation) or associated estimates of uncertainty (e.g. confidence intervals)
☒	☐	For null hypothesis testing, the test statistic (e.g. *F*, *t*, *r*) with confidence intervals, effect sizes, degrees of freedom and *P* value noted *Give P values as exact values whenever suitable.*
☒	☐	For Bayesian analysis, information on the choice of priors and Markov chain Monte Carlo settings
☒	☐	For hierarchical and complex designs, identification of the appropriate level for tests and full reporting of outcomes
☒	☐	Estimates of effect sizes (e.g. Cohen's *d*, Pearson's *r*), indicating how they were calculated

Our web collection on statistics for biologists contains articles on many of the points above.

Software and code

Policy information about availability of computer code

Data collection	SerialEM
Data analysis	CryoSPARC v2.12, Relion v3.0, Chimera v1.15, ChimeraX - Isolde v1.4, Phenix v1.20.1-4489, Coot v0.9.6, MOLE v2, Analyst vTF1.5, MSConvert (ProteoWizard), ProteinProspector v 5.19.1, XLTools, xiNET, Integrative Modeling Platform

For manuscripts utilizing custom algorithms or software that are central to the research but not yet described in published literature, software must be made available to editors and reviewers. We strongly encourage code deposition in a community repository (e.g. GitHub). See the Nature Portfolio guidelines for submitting code & software for further information.

Data

Policy information about availability of data

All manuscripts must include a data availability statement. This statement should provide the following information, where applicable:

- Accession codes, unique identifiers, or web links for publicly available datasets
- A description of any restrictions on data availability
- For clinical datasets or third party data, please ensure that the statement adheres to our policy

all data obtained in this study have been deposited as noted in the manuscript. all data obtained in this study have been deposited as noted in the manuscript. The atomic coordinates for six structures of pks13 have been deposited in the Protein Data Bank with the accession codes 7UK4, 8CUY, 8CV1, 8CUZ, 8CV0. The corresponding maps have been deposited in the Electron Microscopy Data Bank with the accession codes EMD-26574, EMD-27002, EMD27005, EMD-27003,

EMD-27004. Proteomics data have been deposited to the ProteomeXchange Consortium with the dataset identifier PXD033471. Files containing the input data, scripts, and output results for integrative modeling are freely available at https://github.com/integrativemodeling/Pks13. The details about the approach are given in Table S4.

Human research participants

Policy information about studies involving human research participants and Sex and Gender in Research.

Reporting on sex and gender	Not Applicable
Population characteristics	Not Applicable
Recruitment	Not Applicable
Ethics oversight	Not Applicable

Note that full information on the approval of the study protocol must also be provided in the manuscript.

Field-specific reporting

Please select the one below that is the best fit for your research. If you are not sure, read the appropriate sections before making your selection.

☒ Life sciences ☐ Behavioural & social sciences ☐ Ecological, evolutionary & environmental sciences

For a reference copy of the document with all sections, see nature.com/documents/nr-reporting-summary-flat.pdf

Life sciences study design

All studies must disclose on these points even when the disclosure is negative.

Sample size	Several millions of particle images were combined into the CryoEM analysis. They were classified into the different states whose structures are reported.
Data exclusions	As in cryoEM analysis, many thousands of images are classified according to their quality. Those images that do not have suitable quality, or do not fit th eclasses are excluded from further averaging. As to the chemical cross linking, we excluded large molecular weight species that were from potential aggregates of multiple molecules, cross linked residues that are too far apart for within a dimeric Pks13 were excluded since they were presumed to arise from multimeric assemblies of PKS molecules and not relevant to intramolecular dynamics. (detailed in Methods, and Fig S9, S10, and Extended Fig 10.
Replication	he only replication was that the crosslinking experiment was done twice but at two different temperatures, giving non-equivalent data that were not compared statistically. see Supp Fig 9. caption
Randomization	4,400,000 Images of Single particles for the di-domain structures (KS-AT) and 1,200,000 for each of the other 5 structures, were classified according to standard procedures in cryoEM imaging by classification into separate classes that are gleaned from 100% of the particle image sets.
Blinding	There was no blinding. images of particles were picked according to classification into classes as is the standard in cryoEM imaging

Reporting for specific materials, systems and methods

We require information from authors about some types of materials, experimental systems and methods used in many studies. Here, indicate whether each material, system or method listed is relevant to your study. If you are not sure if a list item applies to your research, read the appropriate section before selecting a response.

Materials & experimental systems

n/a	Involved in the study
☒	☐ Antibodies
☒	☐ Eukaryotic cell lines
☒	☐ Palaeontology and archaeology
☒	☐ Animals and other organisms
☒	☐ Clinical data
☒	☐ Dual use research of concern

Methods

n/a	Involved in the study
☒	☐ ChIP-seq
☒	☐ Flow cytometry
☒	☐ MRI-based neuroimaging